

1 **Spatial-temporal changes in flow hydraulic characteristics and soil loss**  
2 **during gully headcut erosion under controlled conditions**

3  
4 Mingming Guo<sup>a</sup>, Zhuoxin Chen<sup>b</sup>, Wenlong Wang<sup>b,c,\*</sup>, Tianchao Wang<sup>d</sup>, Qianhua Shi<sup>b</sup>, Hongliang  
5 Kang<sup>b</sup>, Man Zhao<sup>b</sup>, Lanqian Feng<sup>c</sup>

6  
7 a Key laboratory of Mollisols Agroecology, Northeast Institute of Geography and Agroecology,  
8 Chinese Academy of Sciences, Harbin 150081, Heilongjiang, China

9 b State Key Laboratory of Soil Erosion and Dryland Farming on the Loess Plateau, Institute of Water  
10 and Soil Conservation, Northwest A&F University, Yangling, Shaanxi 712100, China

11 c Institute of Soil and Water Conservation, Chinese Academy of Sciences and Ministry of Water  
12 Resources, Yangling, Shaanxi 712100, China

13 d Ulanyab Grassland Station, Jining, Inner Mongolia 012000, China

14 **\*Corresponding author:** Wenlong Wang

15 E-mail addresses: nwafu\_wwl@163.com; wllwang@nwsuaf.edu.cn

16

## 17 **Abstract**

18 The temporal-spatial changes in flow hydraulics and energy consumption and their associated soil  
19 erosion remain unclear during gully headcut retreat. A simulated scouring experiment was conducted  
20 on five headcut plots consisting of upstream area (UA), gully headwall (GH) and gully bed (GB) to  
21 elucidate the temporal-spatial changes in flow hydraulic, energy consumption, and soil loss during  
22 headcut erosion. The flow velocity at the brink of headcut increased as a power function of time,  
23 whereas the jet velocity entry to plunge pool and jet shear stress logarithmically or linearly decreased  
24 over time. The jet properties were significantly affected by upstream flow discharge. The Reynold  
25 number, runoff shear stress, and stream power of UA and GB increased as logarithmic or power  
26 functions of time, but the Froude number decreased logarithmically over time. The Reynold number,  
27 shear stress and stream power decreased by 56.0%, 63.8% and 55.9%, respectively, but the Froude  
28 number increased by 7.9% when flow dropped from UA to GB. The accumulated energy  
29 consumption of UA, GH and GB positions linearly increased with time. 91.12% - 99.90% of total  
30 flow energy was consumed during headcut erosion, of which the gully head accounted for 77.7% of  
31 total energy dissipation followed by UA (18.3%) and GB (4.0%). The soil loss rate of the  
32 “UA-GH-GB” system initially rose and then gradually declined and levelled off. The soil loss of UA  
33 and GH decreased logarithmically over time, whereas the GB was mainly characterized by sediment  
34 deposition. The proportion of soil loss at UA and GH are 11.5% and 88.5%, respectively, of which  
35 the proportion of deposited sediment on GB reached 3.8%. The change in soil loss of UA, GH and  
36 GB was significantly affected by flow hydraulic and jet properties. The critical energy consumption  
37 initiating soil erosion of UA, GH, and GB are  $1.62 \text{ J s}^{-1}$ ,  $5.79 \text{ J s}^{-1}$  and  $1.64 \text{ J s}^{-1}$ , respectively. These  
38 results are helpful to deepen the understanding of gully erosion process and hydrodynamic  
39 mechanism and also can provide scientific basis for the construction of gully erosion model and the  
40 design of gully erosion prevention measures.

41  
42 **Keywords:** Gully erosion; Hydraulic property; Headcut retreat; Mass failure; Energy dissipation

43

## 44 **1 Introduction**

45 Gully erosion is a typical soil erosion process whereby concentrated runoff from an upstream  
46 drainage area recurs in a channel and erodes soil from the area through which runoff passed to  
47 considerable depth (Poesen et al., 2003; Zhu, 2012). Gully erosion is recognized as the main  
48 sediment source in some hilly and gully-dominated watersheds (Poesen et al., 2003; Valentin et al.,  
49 2005; Dotterweich et al., 2012). Poesen et al. (2003) reported that soil loss amount caused by gully  
50 erosion accounts for 10% - 94% of total soil loss amount based on the collected data from published  
51 articles. Moreover, gully erosion can severely damage to infrastructure, enhance the terrain  
52 fragmentation, and cause ecosystem instability, land degradation and food safety (Vanmaercke et al,  
53 2016; Zhang et al., 2018; Hosseinalizadeh et al., 2019; Arabameri et al., 2020; Bogale et al., 2020;  
54 Belayneh et al., 2020; Wen et al., 2020).

55 As the primary process of the gully erosion, the gully headcut retreat often significantly  
56 influences and determines gully erosion (Oostwoud-Wijdenes et al., 2000; Vandekerckhove et al.,  
57 2003; Guo et al., 2019). A headcut is defined as a vertical or near-vertical drop or discontinuity on  
58 the bed of a gully occurring where flow is concentrated at a knickpoint (Hanson et al., 2001; Bennett  
59 et al., 2000). Many studies have demonstrated that the gully erosion is the result of the combined  
60 actions of plunge pool erosion by jet flow, upstream runoff incision, headwall erosion by on-wall  
61 flow, mass failure (gully head and wall collapse), (Vanmaercke et al., 2016; Addisie et al., 2017; Guo  
62 et al., 2019). Once a headcut is formed in upstream area, the gully will develop rapidly and not stop  
63 forward until a critical topographic condition is formed ( $S \leq a \cdot A^b$ , where  $S$  and  $A$  is the slope gradient  
64 and drainage area upstream gully headcut, respectively) (Kirkby et al., 2003). Moreover, the different  
65 landform units (upstream area, UA; gully head, GH; gully bed, GB) of gully system exhibited  
66 completely different erosion processes and hydrodynamic mechanisms during gully headcut erosion  
67 (Zhang et al., 2018; Guo et al., 2019; Shi et al., 2020a). The combination and interaction of erosion  
68 processes of the three landform units determined gully headcut erosion process (Vanmaercke et al.,  
69 2016). Therefore, clarifying the soil erosion process and characteristics of the three landform units is  
70 critical to systematically and clearly reveal the mechanism of gully headcut erosion.

71 Previous studies suggested that gully heacut erosion is affected by various factors including

72 topography, land use change, vegetation, soil properties, and climate (Vanwallegem et al., 2003;  
73 Ionita, 2006; Rodzik et al., 2009; Rieke-Zapp and Nichols, 2011; Torri and Poesen, 2014; Ionita et al.,  
74 2015; Vannoppen et al., 2015; Guo et al., 2019, 2020a). In terms of topography, most of studies  
75 focused on the threshold relationship ( $S \leq a \cdot A^b$ ) to initiate gully erosion (e.g., Torri and Poesen, 2014).  
76 Several experimental studies demonstrated that the upstream slope gradient and headcut height have  
77 significant effects on headcut erosion (e.g., Bennett, 1999; Zhang et al., 2018). Land use change is  
78 recognized as having the strongest effect on processes related to gully erosion (Poesen et al., 2003;  
79 Chaplot et al., 2005; Descroix et al., 2008), and also significantly affects the activation of gully  
80 headcut erosion (e.g., Torri and Poesen, 2014). In this aspect, the vegetation coverage is a parameter  
81 that is often used to clarify its effect on gully erosion (e.g., De Baets et al., 2007;  
82 Martínez-Casasnovas et al., 2009), however, in fact, the vegetation effect mainly depends on the root  
83 characteristics and its distribution at gully head (e.g., Vannoppen et al., 2015; Guo et al., 2019).  
84 Nevertheless, at present, the most of studies on gully erosion focus on the changes in gully  
85 morphology between different periods at a watershed or regional scale (Vanmaercke et al., 2016),  
86 which is why the previous studies fail to address the effects of root systems on gully headcut retreat.  
87 Guo et al. (2019) concluded that the grass (*Agropyron cristatum*) could reduce soil loss and headcut  
88 retreat distance by 45.6–68.5%, 66.9–85.4%, respectively, compared with bare land, and the roots of  
89 0–0.5 mm in diameter showed the greatest controlling influence on headcut erosion. In terms of soil  
90 properties, lots of studies have proved the significant effect of soil properties on gully headcut  
91 erosion (e.g., Nazari Samani et al., 2010), which is mainly related to the change in soil erodibility  
92 induced by soil properties including soil texture, soil vertical joints, soluble mineral content, soil  
93 lithology, and physicochemical properties (Sanchis et al., 2008; Vanmaercke et al., 2016; Guo et al.,  
94 2020a). Rainfall, the main climate factor, is closely related to runoff generation and thus be expected  
95 to affect headcut erosion. Many studies have reported that the initiation of gully headcut is correlated  
96 with rainfall characteristics (e.g., summation of rainfall from 24-hour rains equal to or greater than  
97 0.5 inches) (Beer and Johnson, 1963; Vandekerckhove et al., 2003; Rieke-Zapp and Nichols, 2011).  
98 However, the great difference in the threshold value relating to rainfall factors was found among  
99 different areas of the world due to fully different erosion environments. For example, in the northeast

100 of China, the gully erosion is the result of soil thawing, rainfall runoff and snowmelt runoff (Li et al.,  
101 2016b; Xu et al., 2019). Furthermore, at present, the most of studies on gully erosion were conducted  
102 to quantify the change in gully erosion (retreat rate, area and volume) at different spatial and  
103 temporal scales by using remote sensing interpretation, real-time monitoring and meta-analysis based  
104 on literature data (e.g., Vanmaercke et al., 2016). However, the influencing mechanism of these  
105 factors on gully headcut erosion is still unclear and need to be revealed in future studies.

106 Evidently, the concentrated flow upstream gully head, mainly depended on the drainage area  
107 upstream gully heads and rainfall characteristics, is the main and original drive force triggering  
108 headcut erosion. The runoff firstly eroded the upstream area and then was parted into two types of  
109 flow (on-wall flow and jet flow) at the brinkpoint of gully headcut (Guo et al., 2021a). Consequently,  
110 the on-wall flow persistently eroded the headwall soil, and the jet flow violently impacted gully bed  
111 soil and formed a plunge pool (Su et al., 2015; Guo et al., 2019). Subsequently, the two types of flow  
112 merged again and eroded gully bed together (Zhang et al., 2018; Shi et al., 2020a). The runoff  
113 hydraulic or jet flow properties at different landform units (upstream area, gully head and gully bed)  
114 are significantly different, which is an important reason for the difference in erosion process among  
115 different landform units. However, the temporal-spatial change in runoff and jet properties during  
116 headcut erosion is still unclear and thus needs to be clarified. Furthermore, at present, some  
117 experimental studies on headcut erosion of rill, ephemeral gully, gully and bank gully were  
118 conducted to investigate the runoff properties, energy consumption, sediment transport process,  
119 morphology evolution and empirical model (Bennett and Casali, 2001; Wells et al., 2009a, 2009b; Su  
120 et al., 2014; Xu et al., 2017a; Guo et al., 2019; Shi et al., 2020a). However, relatively few  
121 knowledges were obtained to systemically reveal the hydrodynamic mechanism of gully headcut  
122 erosion. Therefore, elucidating the temporal-spatial changes in runoff hydraulic and soil loss and  
123 hydrodynamic mechanism of UA, GH and GB is of great importance to systematically reveal the  
124 hydrodynamics mechanism of gully headcut erosion.

125 Given the above-mentioned issues, a series of simulated gully headcut erosion experiments  
126 subjected to inflow scouring are conducted to (1) investigate the temporal-spatial change in runoff  
127 hydraulic and jet flow properties during headcut erosion, (2) quantify the dynamic change of energy

128 consumption and soil loss and their spatial distribution, and (3) reveal the erosion hydrodynamic  
129 mechanism of UA, GH and GB.

## 130 **2 Materials and Methods**

### 131 **2.1 Study area**

132 This experiment was carried out at the Xifeng Soil and Water Conservation Experimental  
133 Station that is located in the Nanxiaohegou watershed, Qingyang City, Gansu Province, China. The  
134 study area belongs to a semi-arid continental climate with a mean annual temperature of 9.3 °C. The  
135 mean annual precipitation is 546.8 mm (1954 - 2014), of which precipitation from May to September  
136 accounts for 76.9% of the total precipitation (Xia et al., 2017; Guo et al., 2019). The elevation ranges  
137 from 1050 to 1423 m. The main landforms include gentle loess-tableland, steep hillslope and gully  
138 channel, and their areas account for 57.0%, 15.7% and 27.3%, respectively. The loess-tableland is  
139 characterized by low slope (1–5°), gentle and flat terrain and fertile soil. The main soil type is  
140 loessial soil with silt loam texture. Most of hillslopes have been constructed as slope-terraces. The  
141 main gully channel is usually U-shaped and the branch-gully is more actively developed and easily  
142 eroded as a V-shaped by runoff from loess-tableland (Xu et al., 2019). The flat loess-tableland can  
143 accumulate the 67.4% of total runoff and cause serious gully erosion that can contribute 86.3% of the  
144 total soil erosion (Guo et al., 2019). The original plant species have been seriously destroyed. Since  
145 the 1970s, the “Three Protection Belts” system, the “Four Eco-Economical Belts” system and the  
146 “Grain for Green” project (Zhao, 1994; Fu et al., 2011) were implemented to control soil erosion.  
147 The main land use on loess-tableland position has always been farmland and orchards, while the land  
148 use on hillslope is sloping farmland and orchards before 1999, which have been changed into  
149 forested and grassy land due to the “Grain for Green” project. The current mean annual soil erosion  
150 rate has been reduced to 4350 Mg km<sup>-2</sup> y<sup>-1</sup> in the study watershed (Guo et al., 2019). The plants are  
151 primarily artificially planted arbors and herbaceous vegetation and shrubs (Guo et al., 2021b).

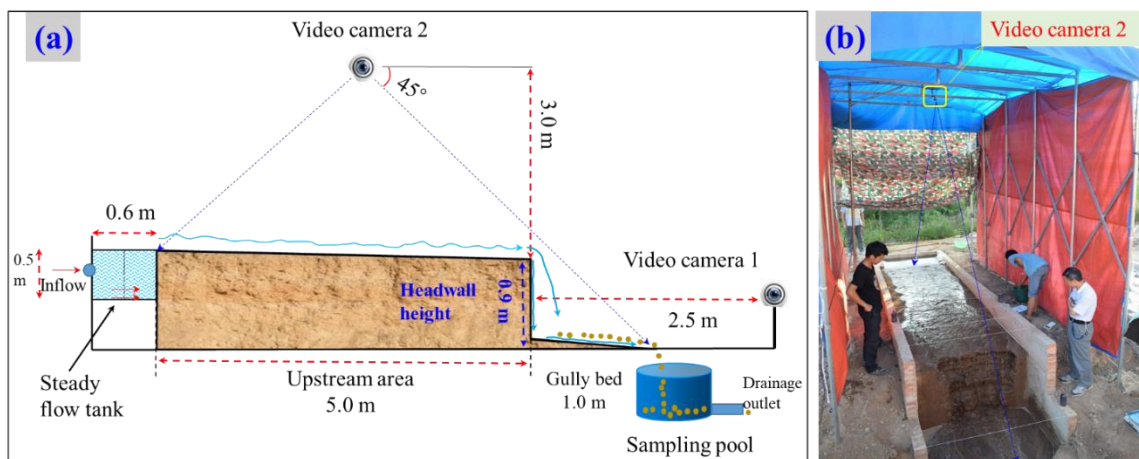
152

### 153 **2.2 Experimental design**

#### 154 **2.2.1 Gully head experimental plot construction**

155 Five gully head plots for headcut erosion experiments were constructed at the experimental

156 station in April 2018. Fig. 1 shows the basic information of the gully head plot consisting of three  
 157 landform units (upstream area, headwall and gully bed). The plot width and slope gradient of  
 158 upstream area and gully bed are uniformly designed as 1.5 m and 3°, respectively. The upstream area  
 159 length, the height of the vertical headwall and the length of the gully bed are 5.0 m long, 0.9 m, and  
 160 1.0 m, respectively (Fig. 1a). The plot boundary was constructed in strict accordance with designed  
 161 plot dimension using cement and bricks (Fig. 1b). After the construction of plot boundary, the soil  
 162 was sieved through a 2 cm sieve with to remove roots and debris and ensure uniform soil underlying  
 163 condition. The sieved soil was filled into the plot every 10-cm thick layer according to the  
 164 investigated soil bulk density of gully heads. The soil surface of each layer was harrowed to increase  
 165 the cohesion between two soil layers (Guo et al., 2019). In general, the filling upstream area length  
 166 was 5.5 m that was larger than the precise upstream area length (5.0 m). After establishment of gully  
 167 head plots, the five plots were carefully managed about four months (August 2018) to allow the soil  
 168 to return to its nearly natural state. During the four-month conservation process, the naturally  
 169 growing weeds were weeded out in time. Moreover, a flow-steady tank of 0.6 m, 1.5 m and 0.5 m in  
 170 length, width and height was installed at the top of upstream area, and a circular sampling pool of 0.6  
 171 m in diameter was set at the bottom of the gully bed to collect runoff and sediment (Fig. 1a).  
 172 According to the pre-experimental results, the length of upstream area can meet the needs of headcut  
 173 migration under designed flow discharge ( $3.0 - 7.2 \text{ m}^3 \text{ h}^{-1}$ ) and gully head height (0.9 m), and the  
 174 length of gully bed also can satisfy the development of plunge pool by jet flow and stabilize the flow  
 175 of gully bed.



176  
 177 **Figure 1** Sketch (a) and photo (b) of experimental plot.

178

## 179 **2.2.2 Inflow discharge design**

180 The concentrated runoff generated from upstream area is the main force driving gully headcut  
181 erosion. Jiao et al (1999) concluded that the more serious soil erosion is generally caused by “A”  
182 type rainstorm with the rainfall duration of 25 to 178 mins than other types of rainstorms in the Loess  
183 Plateau. Thus, an extreme case of rainfall duration (180 min) was considered in this study, and the  
184 recurrence period of “A” type rainstorm was designed as 30 years. Previous studies indicated that the  
185 rainstorm distribution on the Loess Plateau showed a non-significant change in past decades (Li et al.,  
186 2010; Sun et al., 2016; Wen et al., 2017). Zhang et al. (1983) proposed a statistical equation (Eq. (1))  
187 for calculating the average rainfall intensity by analyzing 1710 typical rainstorm events in the Loess  
188 Plateau. Then, the inflow discharge was calculated by Eq. (2) that involves the runoff coefficient,  
189 storm intensity and drainage area upstream gully head and ranged from 3.12 to 9.68 m<sup>3</sup> h<sup>-1</sup>. Before  
190 the study, we first conducted some preliminary experiments under some flow discharges, and  
191 meanwhile considering the pre-experiment effect, finally, we selected the five inflow discharge levels  
192 (3.0, 3.6, 4.8, 6.0, and 7.2 m<sup>3</sup> h<sup>-1</sup>).

$$193 \quad RI = \frac{5.09N^{0.379}}{(t+1.4)^{0.74}} \quad (1)$$

194 where  $RI$  is the average rainfall intensity during  $t$  minutes, mm min<sup>-1</sup>;  $N$  is the recurrence period  
195 of rainstorm, yr; and  $t$  is the rainfall duration, min.

$$196 \quad q = \frac{60\alpha \cdot A \cdot RI \cdot w}{W} \quad (2)$$

197 where  $A$  is the upstream area (km<sup>2</sup>) and has a wide range of 0.15 - 8.7 km<sup>2</sup> according to an early  
198 investigation of research team (Che, 2012);  $W$  is the width of the upstream area, km;  $w$  is the plot  
199 width, m; and  $\alpha$  is the runoff coefficient of bare land and is identified as 0.167 by analyzing the  
200 runoff and rainfall data of standard runoff plots (Li et al., 2006).

## 201 **2.3 Experimental procedure**

202 The scouring experiment was conducted in August 2018. Before formal experiment, the  
203 upstream area length was firstly adjusted to designed length of 5.0 m (Fig. 2a). Then, a self-made  
204 tent (length × width × height: 6.0 m × 3.0 m × 3.5 m) with waterproof canvas enclosed the plot to  
205 resist the effects of natural rainfall and sunshine on experimental progress and photo shooting for 3D



206 reconstruction (Fig. 1b). In addition, the experimental process was recorded by two Logitech 930e  
207 video cameras with a resolution of 2.0 megapixels. The camera 1 was installed 2.5 m in front of plot  
208 headwall (Fig. 1a), and the camera 2 was installed 3.0 m above the plot center (Fig. 1a).

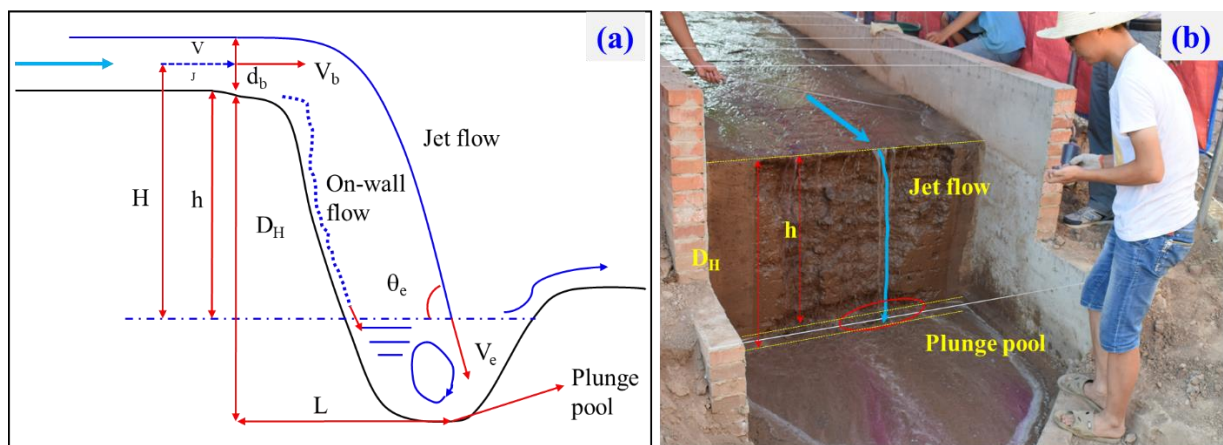
209 Before the experiment, watering can be used to spray each experimental plot until surface runoff  
210 was generated, and then the plot was placed for 24 hours to ensure adequate water infiltration, which  
211 can assure that the soil moisture of the five plots was approximately the same. The inlet pipeline was  
212 placed in steady flow tank when the inflow discharge was adjusted to designed value. A water  
213 thermometer was placed into the steady flow tank to monitor the change in water temperature during  
214 experiments. The runoff and sediment samples at the plot outlet were collected at 2-min intervals to  
215 represent the temporal change in runoff and sediment of “UA – GH – GB” system, and the sampling  
216 time was recorded using a stopwatch (Fig. 2b). The runoff and sediment samples were oven-dried at  
217 105 °C for 24 h and weighed to calculate the soil loss rate of “UA – GH – GB” system. Besides, the  
218 timing of the collapse event was recorded during headcut erosion. The upstream area was divided  
219 into 4 runoff observation sections, and the runoff width ( $w$ ), depth ( $d$ ) and velocity ( $V$ ) of each  
220 section were measured by a calibrated scale of 1 mm accuracy and color tracer method (Fig. 2b, 2c).  
221 The runoff velocity ( $V_j$ ) before runoff arrived at the brink of headcut was measured 5 – 8 times by  
222 the flow velocity measuring instrument (LS300-A). The instrument was firstly placed perpendicular  
223 to the flow section but does not touch the underlying surface. When the flow passes through the  
224 turbine, the flow velocity can be measured by the rotating velocity of the turbine with the accuracy of  
225  $0.01 \text{ m s}^{-1}$  and measuring error of  $< 1.5\%$ , and the runoff width at the headcut brinkpoint was  
226 measured (Fig. 2d). The runoff width and velocity of gully bed were also measured using the same  
227 method with upstream area (Fig. 2e). Above mentioned measurements of runoff characteristics and  
228 sediment samples were finished in 2-min intervals. The whole experimental process was recorded by  
229 two video cameras and imported into computers (Fig. 2f). In addition to above runoff parameters, the  
230 runoff depth ( $d_b$ ) at the brink of headcut, the plunge pool depth ( $D_H$ ) and the vertical distance ( $h$ )  
231 from brink-point of headcut to water surface of plunge pool were also measured 3 - 5 times by a steel  
232 ruler with 1 mm accuracy within each 2-min intervals (Fig. 3).



233

234

**Figure 2** Runoff and sediment observation and recoding at upstream area, gully head and gully bed.



235

236

**Figure 3** Sketch of jet flow at gully headcut and plunge pool at gully bed.

237

238

239

240

241

242

243

244

245

246

To obtain the dynamic change in morphology of erosional landform during gully headcut erosion, the experimental duration (180 min) was divided into six stage (30 – 60 – 90 – 120 – 150 – 180 min). Photo-based three-dimensional (3D) reconstruction method was employed to obtain the digital elevation model (DEM) data of each plot prior to experiment and after each 30-min test. A total of 14 target points were placed around the plot for identifying the 3D coordinate before the photos were taken. The eroded photographic was recorded by a Nikon D5300 camera with the focal length of 50 mm. The following aspects were required during photos shooting: (1) obvious water on soil surface and direct sunshine should be avoided, (2) a minimum overlap of 60% between subsequent photographs was required, and (3) some complex eroded photographic should be taken in detail. In this study, the upper left corner of the plot was set as the original coordinates (0, 0, 0), and

247 the direction of three-dimensional coordinate was determined as shown in Fig. 3d. These collected  
 248 photos were imported in Agisoft PhotoScan software (Agisoft LLC, Russia, professional version  
 249 1.1.6), and then these control points and their coordinates would be identified and entered into the  
 250 software. The root mean square errors for the altitudes (Z axis) of the target points are 0.0037, 0.0045,  
 251 0.0024, 0.0052 and 0.0030 m on average, respectively, for the experiments of five inflow discharges,  
 252 which can satisfy the study requirement (millimeter level). The DEM could be exported and was  
 253 used to extract the morphological parameters and soil loss volume of three landform units at six  
 254 stages (Frankl et al., 2015).

## 255 **2.4 Parameter calculation, data analysis and figure plotting**

### 256 **2.4.1 Hydraulic parameters of upstream area and gully bed**

257 Five parameters including runoff velocity ( $V$ , m s<sup>-1</sup>), Reynold number ( $Re$ ), Froude number ( $Fr$ ),  
 258 shear stress ( $\tau$ , Pa) and stream power ( $\omega$ , W m<sup>-2</sup>) were used to characterize the changes in hydraulic  
 259 properties at upstream area and gully bed positions. The several parameters except for  $V$  are  
 260 calculated as follows.

$$261 \quad Re = \frac{V \cdot R}{\nu} \quad (1)$$

$$262 \quad Fr = \frac{V}{\sqrt{g \cdot R}} \quad (2)$$

$$263 \quad R = \frac{w \cdot d}{w + 2d}, \nu = \frac{1.775 \times 10^{-6}}{1 + 0.0337T + 0.000221T^2} \quad (3)$$

$$264 \quad \tau = \rho_w \cdot g \cdot R \cdot J \quad (4)$$

$$265 \quad \omega = \tau \cdot V \quad (5)$$

266 where  $R$  (m) and  $\nu$  (m<sup>2</sup> s<sup>-1</sup>) are the hydraulic radius and the water kinematic viscosity coefficient,  
 267 respectively;  $w$  (m),  $d$  (m) and  $T$  (°C) are the runoff width, depth and water temperature, respectively;  
 268  $\rho_w$  (kg m<sup>-3</sup>) is the water density and  $J$  (m m<sup>-1</sup>) is the hydraulic gradient.

### 269 **2.4.2 Jet properties of gully head**

270 Based on the measured runoff velocity ( $V_J$ , m s<sup>-1</sup>) before runoff arrived at the headcut brinkpoint,  
 271 the runoff depth ( $d_b$ , m) at the headcut brinkpoint, the plunge pool depth ( $D_H$ , m) and the vertical  
 272 distance ( $h$ , m) (Fig. 3a), the three parameters including the runoff velocity at the headcut brinkpoint  
 273 ( $V_b$ ), jet-flow velocity entry to plunge pool ( $V_e$ ) and jet-flow shear stress ( $\tau_j$ ) were calculated to

274 clarify the change of jet properties (Rouse, 1950; Hager, 1983; Stein et al., 1993; Flores-Cervantes et  
 275 al., 2006; Zhang et al., 2016). The three parameters were calculated as follows.

$$276 \quad V_b = \begin{cases} \frac{\sqrt[3]{q \cdot g}}{0.715}, Fr < 1 \\ V_J \cdot \frac{Fr^2 + 0.4}{Fr^2}, Fr > 1 \end{cases} \quad (5)$$

$$277 \quad Fr = \frac{V_J}{\sqrt{g \cdot d_b}} \quad (6)$$

$$278 \quad V_e = \frac{V_b}{\cos \theta_e}, \theta_e = \arctan \left( \frac{\sqrt{2g \cdot D_H}}{V_b} \right) \quad (7)$$

$$279 \quad \tau_j = 0.025 \left( \frac{v}{q} \right)^{0.2} \cdot \rho_w \cdot [2g \cdot (h + d_b/2) + V_b^2] \quad (8)$$

### 280 **2.4.3 Energy consumption of upstream area, gully head and gully bed**

281 In this study, energy consumption of three landform units (upstream area, UA; gully head, GH;  
 282 gully bed, GB) were calculated according to the measured runoff characteristic parameters. The  
 283 bottom of GB was treated as the zero potential surface to quantify the energy consumption.  
 284 Therefore, the total runoff energy ( $E_T$ , J s<sup>-1</sup>), the runoff energy at the brink of headcut ( $E_L$ , J s<sup>-1</sup>), the  
 285 runoff energy when runoff leaves the plunge pool ( $E_H$ , J s<sup>-1</sup>), and the runoff energy at the bottom of  
 286 gully bed ( $E_B$ , J s<sup>-1</sup>) were calculated as following. The calculation was consistent with the theory of  
 287 minimum rate of energy dissipation expressed by Yang (1971a, 1971b).

$$288 \quad E_T = \rho_w g q [(L_l + L_g) \tan \theta + H_h] \quad (9)$$

$$289 \quad E_L = \rho_w g q [(L_m + L_g) \tan \theta + H_h] + \frac{1}{2} \rho_w q V_J^2 \quad (10)$$

$$290 \quad E_H = \rho_w g q \left( L_m + L_g - V_b \sqrt{\frac{2h}{g}} \right) \tan \theta + \frac{1}{2} \rho_w q V_P^2 \quad (11)$$

$$291 \quad E_B = \frac{1}{2} \rho_w q V_B^2 \quad (12)$$

292 where the  $L_l$  (m) and  $L_g$  (m) are the projection length of UA and GB, respectively, during gully  
 293 head migration;  $L_m$  (m) is the gully head retreat distance;  $H_h$  (m) is the initial gully headcut height.  
 294  $V_P$  (m s<sup>-1</sup>) and  $V_B$  (m s<sup>-1</sup>) are the runoff velocity runoff leaving the plunge pool and GB, respectively.

295 Therefore, the total runoff energy consumption ( $\Delta E_T$ , J s<sup>-1</sup>), the runoff energy consumption of  
 296 UA ( $\Delta E_L$ , J s<sup>-1</sup>), the runoff energy consumption of GH ( $\Delta E_H$ , J s<sup>-1</sup>) and the runoff energy consumption  
 297 of GB ( $\Delta E_B$ , J s<sup>-1</sup>) could be calculated as follows.

$$298 \quad \Delta E_T = E_T - E_B \quad (13)$$

299 
$$\Delta E_L = E_T - E_L \quad (14)$$

300 
$$\Delta E_H = E_L - E_H \quad (15)$$

301 
$$\Delta E_B = E_H - E_B \quad (16)$$

## 302 **2.4.4 Statistical analysis**

303 The curve regression analysis method was employed to determine the quantitative relations  
304 between hydraulic characteristics, jet properties, runoff energy consumption and soil erosion rate and  
305 inflow discharge. The fitted equations between soil loss rate of three landform units and hydraulic  
306 characteristics, jet properties, and energy consumption were also quantified by the curve regression.  
307 The soil erosion volume of upstream area, gully head and gully bed were derived from the DEM of  
308 different stages through the ArcGIS 10.0 software. The data analyse was executed by using SPSS  
309 software (version 6.0) and figure plotting was carried out with Origin 8.5 and PowerPoint 2016  
310 software.

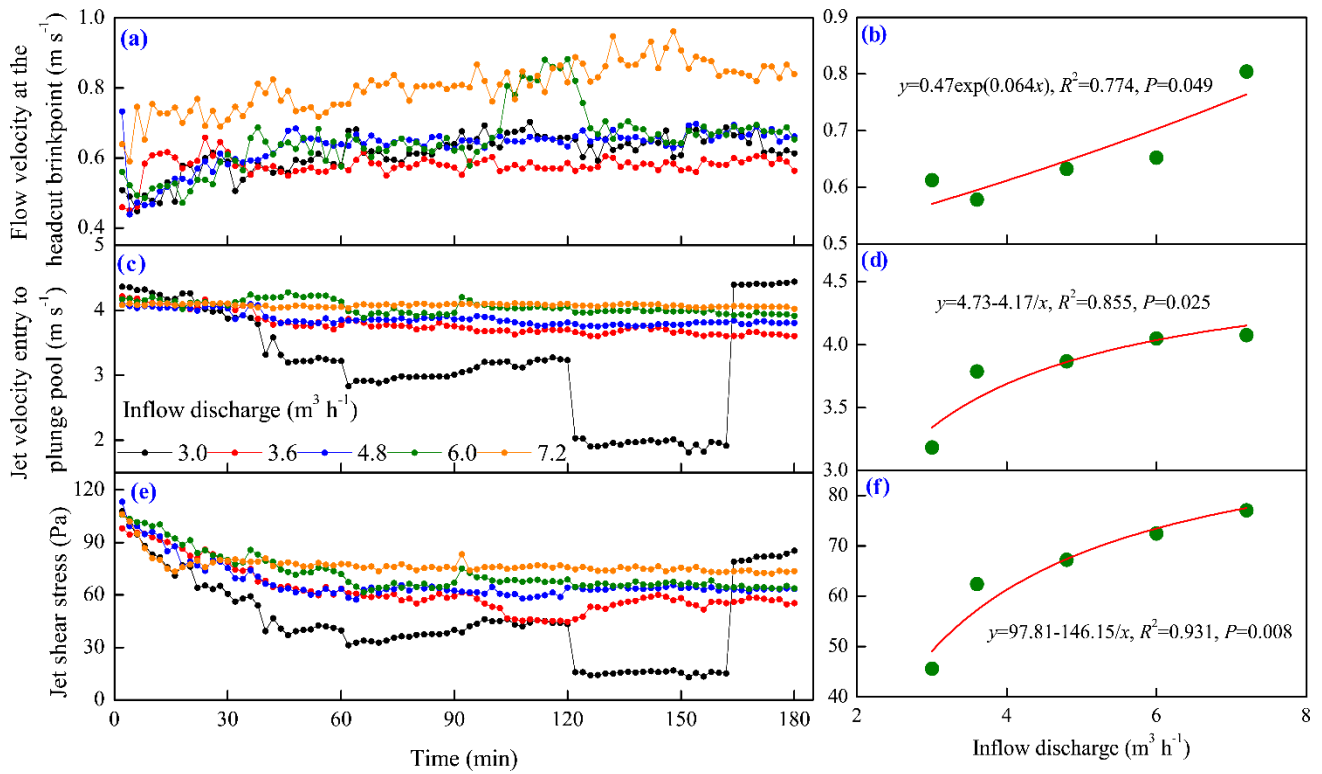
## 311 **3 Results**

### 312 **3.1 Spatial-temporal changes in jet properties and runoff hydraulic**

#### 313 **3.1.1 Jet properties of gully head**

314 Fig. 4 shows the temporal change in the three jet property parameters of gully head (GH) under  
315 different inflow discharge conditions. Overall, the flow velocity at the headcut brinkpoint ( $V_b$ )  
316 increased obviously in the first 30 min and then showed a gradually stable tendency with some  
317 degree of fluctuation (Fig. 4a), and the fluctuation degree was enhanced by the increased inflow  
318 discharge. For example, the  $V_b$  increased sharply from 0.66 to 0.88 m s<sup>-1</sup> during 100 – 124 min under  
319 6.0 m<sup>3</sup> h<sup>-1</sup> inflow discharge due to the headwall failure near headcut enhancing the runoff turbulence.  
320 Regression analysis revealed the significant power relationships ( $V_b = a \cdot t^b$ ,  $R^2 = 0.139 - 0.704$ ,  $P < 0.01$ )  
321 between  $V_b$  and time ( $t$ ) (Table 1). Furthermore, except for 3.6 m<sup>3</sup> h<sup>-1</sup> condition, the  $a$ -value increased  
322 with the inflow discharge increased, but the  $b$ -value showed a weak variation (0.08 - 0.10),  
323 indicating that the flow drainage from gully head can improve initial  $V_b$  but not change its change  
324 trend over time. The mean  $V_b$  exhibited a significantly exponential relationship with inflow discharge  
325 (Fig. 4b,  $P < 0.05$ ). Contrary to the  $V_b$ , the jet velocity entry to plunge pool ( $V_e$ ) and the jet shear stress  
326 ( $\tau_j$ ) experienced a gradually decreased trend with time (Fig. 4c, 4e). Notably, the  $V_e$  and  $\tau_j$  suddenly

327 decreased at 120th min and lasted nearly 40 minutes under  $3.0 \text{ m}^3 \text{ h}^{-1}$  inflow discharge, which was  
 328 mainly attributed to the developed second headcut shortening the jet-flow height. The temporal  
 329 change of  $V_e$  could be described by logarithmic functions under  $3.0 - 4.8 \text{ m}^3 \text{ h}^{-1}$  inflow discharges,  
 330 and expressed by linear functions under the other inflow discharges, whereas the decrease of the  $\tau_j$   
 331 with time could be presented by logarithmic functions under all inflow discharge conditions (Table  
 332 1). Furthermore, both of mean  $V_e$  and  $\tau_j$  could be expressed by a positive “S” function of inflow  
 333 discharge (Fig. 4d, 4f).



334 **Figure 4** Temporal changes in jet properties of headcut and their relationships with inflow discharge.

335 **Table 1** The relationships between jet properties of gully headcut and time.

336

| Inflow discharge<br>( $\text{m}^3 \text{ h}^{-1}$ ) | $V_b \sim t$                       | $V_e \sim t$                                    | $\tau_j \sim t$                             |
|---|------------------------------------|---|---|
| 3.0   | $V_b=0.42t^{0.09}, R^2=0.691^{**}$ | $V_e=5.28-0.49\lg(t), R^2=0.290^{**}$           | $\tau_j=110.86-15.44\lg(t), R^2=0.344^{**}$ |
| 3.6   | $V_b=0.53t^{0.02}, R^2=0.139^{**}$ | $V_e=4.52-0.17\lg(t), R^2=0.859^{**}$           | $\tau_j=117.93-13.14\lg(t), R^2=0.823^{**}$ |
| 4.8   | $V_b=0.46t^{0.08}, R^2=0.544^{**}$ | $V_e=4.25-0.09\lg(t), R^2=0.718^{**}$           | $\tau_j=109.22-9.93\lg(t), R^2=0.770^{**}$  |
| 6.0   | $V_b=0.52t^{0.10}, R^2=0.509^{**}$ | $V_e=4.17-1.33 \times 10^{-3}t, R^2=0.478^{**}$ | $\tau_j=118.73-10.96\lg(t), R^2=0.876^{**}$ |
| 7.2   | $V_b=0.57t^{0.08}, R^2=0.704^{**}$ | $V_e=4.09-1.38 \times 10^{-4}t, R^2=0.111^{**}$ | $\tau_j=95.68-4.42\lg(t), R^2=0.619^{**}$   |

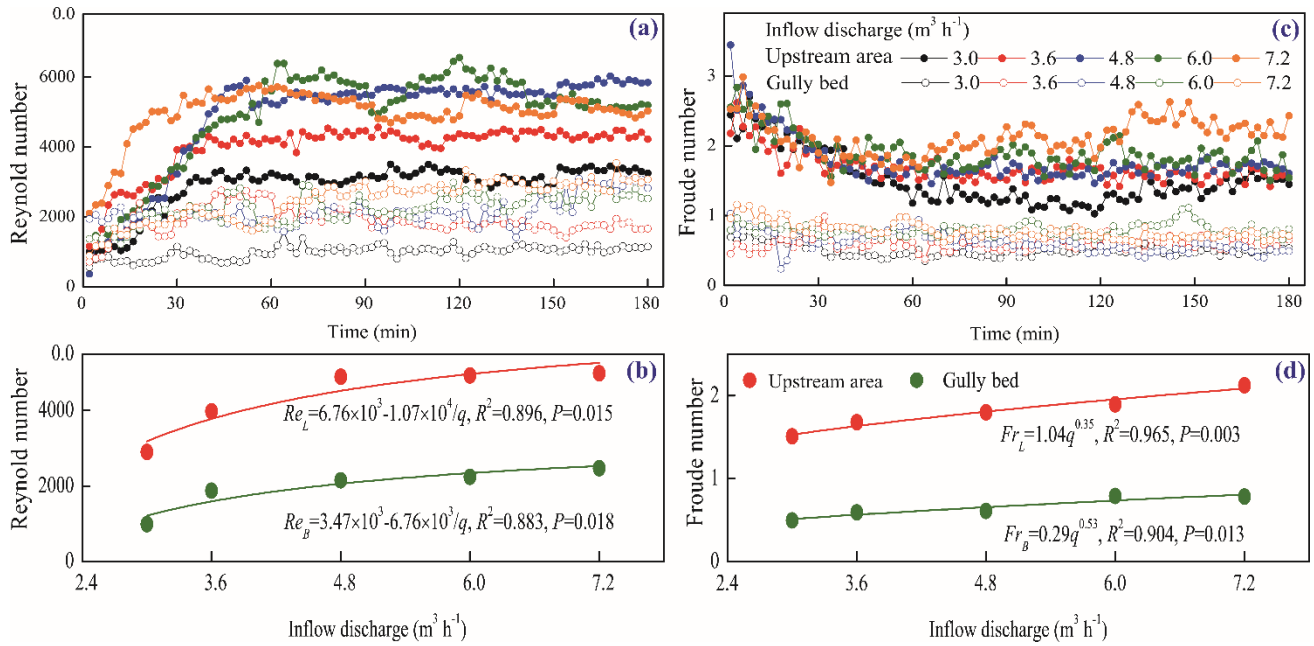
337 Note:  $V_b$ ,  $V_e$  and  $\tau_j$  are runoff velocity at the headcut brinkpoint, runoff velocity entry to plunge pool and the jet  
 338 shear stress, respectively.  $^{**}$  refers to the significance of 0.01. The sample number is 90 for the fitted equations.

### 339 3.1.2 Runoff regime of upstream area and gully bed

340 The temporal changes in runoff Reynold number ( $Re$ ) and Froude number ( $Fr$ ) of upstream area  
341 (UA) and gully bed (GB) and their relationships with inflow discharge are provided in Fig. 5. The  $Re$   
342 of UA and GB showed a similar trend over time, that is, the  $Re$  firstly increased in the first 40 min  
343 and then gradually stabilized (Fig. 5a). In addition, the  $Re$  of UA was larger than that of GB at any  
344 time under same inflow discharge, indicating that the runoff turbulence became weaker after the  
345 runoff of UA passed the gully head. The temporal variation in  $Re$  of UA could be described by  
346 logarithmic and power functions, but, for the GB, the relationship was mainly dominated by power  
347 function (Table 2). On average, the  $Re$  of GB was 50.5% - 65.9% less than that of UA, and the  $Re$  of  
348 UA and GB both increased with the increase of inflow discharge as a power function (Fig. 5b).  
349 However, as illustrated in Fig. 5c, the  $Fr$  experienced a completely opposite trend to  $Re$ . The  $Fr$  of  
350 UA decreased in the first 60 min and then gradually stabilized, but the  $Fr$  of GB experienced a  
351 relatively weak-fluctuating variation over time. For the most of cases, the change in  $Fr$  of UA and  
352 GB over time could be expressed by logarithmic functions (Table 2). On average, the  $Fr$  of UA was  
353 2.39-3.04 times that of GB for same inflow discharge, and the positive power function could describe  
354 the relationship between  $Fr$  and inflow discharge (Fig. 5d).

355 Furthermore, the knowledge of open channel hydraulics is adopted to investigate the difference  
356 in runoff regime between UA and GB. The specific definition is: the flow belongs to laminar when  
357  $Re$  is less than 500, the flow is turbulent when  $Re$  is larger than 2000, and the flow indicates  
358 transitional when  $Re$  ranges from 500 to 2000; and  $Fr = 1$  is the critical value for to distinguish the  
359 subcritical and supercritical flow. The six flow regime zones were divided by three boundary lines  
360 ( $Re = 500$ ,  $Re = 2000$ , and  $Fr = 1$ ) according to the logarithmic relationship between the flow  
361 velocity and hydraulic radius (Fig. 6) (Xu et al., 2017b; Guo et al., 2020b). As shown, the runoff  
362 regimes of UA and GB were located in five entirely different zones. The flow of UA was in the  
363 supercritical-transition flow regime in the first 26 min and then gradually transformed to  
364 supercritical-turbulent flow regime under  $3.0 - 6.0 \text{ m}^3 \text{ h}^{-1}$  inflow discharge, but the flow was always  
365 in the supercritical-turbulent regime zone under  $7.2 \text{ m}^3 \text{ h}^{-1}$  inflow discharge. Moreover, the higher  
366 inflow discharge would enhance the flow turbulent degree. The flow of GB belonged to

367 subcritical-laminar flow category in the initial 6 min, and then transformed to subcritical-transition  
 368 and subcritical-turbulent flow regime when inflow discharge was 3.0 and 3.6 m<sup>3</sup> h<sup>-1</sup>. The flow was in  
 369 the subcritical-turbulent flow regime in most of experimental duration when the inflow discharge  
 370 was 4.8 – 7.2 m<sup>3</sup> h<sup>-1</sup>. The difference in flow regime between UA and GB also indicated that the  
 371 presence of gully head can greatly reduce flow turbulence.



372  
 373 **Figure 5** Temporal changes in runoff regime of upstream area and gully bed and their relationships with inflow  
 374 discharge.  
 375

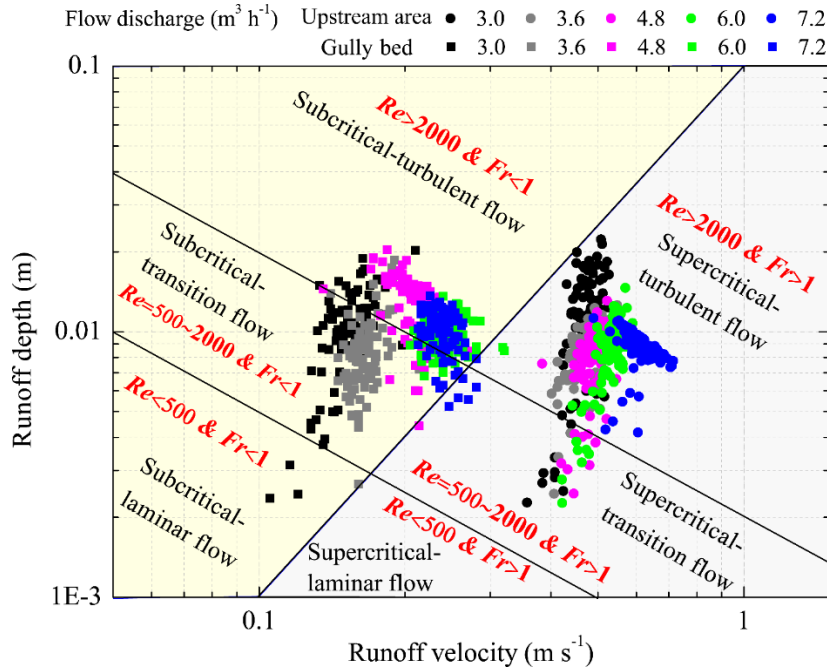
**Table 2** Relationships between runoff hydraulic parameters and time.

| Variable          | Landfor<br>m unit | Inflow discharge (m <sup>3</sup> h <sup>-1</sup> ) |   |   |  |   |
|-------------------|-------------------|--|---|---|--|---|
|                   |                   | 3.0  | 3.6   | 4.8   | 6.0  | 7.2   |
| Reynold<br>number | UA                | $Re=618.691g(t)$<br>$+286.69, R^2=0.761^{**}$      | $Re=705.931g(t)$<br>$+1006, R^2=0.815^{**}$   | $Re=14331g(t)$<br>$-1159, R^2=0.849^{**}$     | $Re=946.64t^{0.38}$ ,<br>$R^2=0.794^{**}$            | $Re=2760t^{0.14}$ ,<br>$R^2=0.486^{**}$       |
|                   | GB                | $Re=514.36t^{0.15}$ ,<br>$R^2=0.504^{**}$          | —   | $Re=4.31t+1760$ ,<br>$R^2=0.334^{**}$         | $Re=1.12 \times 10^3 t^{0.16}$ ,<br>$R^2=0.566^{**}$ | $Re=744.99t^{0.28}$ ,<br>$R^2=0.872^{**}$     |
| Froude<br>number  | UA                | $Fr=2.89-0.331g(t)$ ,<br>$R^2=0.651^{**}$          | $Fr=2.46-0.191g(t)$ ,<br>$R^2=0.651^{**}$     | $Fr=3.27-0.351g(t)$ ,<br>$R^2=0.656^{**}$     | $Fr=2.76-0.201g(t)$ ,<br>$R^2=0.515^{**}$            | —   |
|                   | GB                | $Fr=0.72-0.051g(t)$ ,<br>$R^2=0.326^{**}$          | —   | $Fr=1.0-0.091g(t)$ ,<br>$R^2=0.359^{**}$      | —  | $Fr=1.21-0.101g(t)$ ,<br>$R^2=0.634^{**}$     |
| Shear<br>stress   | UA                | $\tau=0.661g(t)+0.55$ ,<br>$R^2=0.737^{**}$        | $\tau=1.181g(t)+0.78$ ,<br>$R^2=0.813^{**}$   | $\tau=1.321g(t)-0.62$ ,<br>$R^2=0.817^{**}$   | $\tau=1.501g(t)-0.63$ ,<br>$R^2=0.663^{**}$          | $\tau=1.111g(t)+0.99$ ,<br>$R^2=0.819^{**}$   |
|                   | GB                | $\tau=2.44t^{0.08}$ ,<br>$R^2=0.205^{**}$          | $\tau=3.88t^{0.05}$ ,<br>$R^2=0.106^{**}$     | $\tau=2.27t^{0.19}$ ,<br>$R^2=0.664^{**}$     | $\tau=3.64t^{0.12}$ ,<br>$R^2=0.212^{**}$            | $\tau=1.99t^{0.27}$ ,<br>$R^2=0.686^{**}$     |
| Stream<br>power   | UA                | $\omega=0.341g(t)+0.16$ ,<br>$R^2=0.761^{**}$      | $\omega=0.381g(t)+0.55$ ,<br>$R^2=0.815^{**}$ | $\omega=0.781g(t)-0.63$ ,<br>$R^2=0.849^{**}$ | $\omega=0.691g(t)-0.23$ ,<br>$R^2=0.737^{**}$        | $\omega=0.271g(t)+1.56$ ,<br>$R^2=0.436^{**}$ |
|                   | GB                | $\omega=0.28t^{0.15}$ ,<br>$R^2=0.205^{**}$        | $\omega=0.69t^{0.09}$ ,<br>$R^2=0.106^{**}$   | $\omega=0.50t^{0.19}$ ,<br>$R^2=0.664^{**}$   | $\omega=0.83t^{0.09}$ ,<br>$R^2=0.212^{**}$          | $\omega=0.51t^{0.23}$ ,<br>$R^2=0.686^{**}$   |



$R^2=0.504^{**}$  $R^2=0.123^{**}$  $R^2=0.540^{**}$  $R^2=0.338^{**}$  $R^2=0.806^{**}$ 

376 Note: UA and GB refer to upstream area and gully bed.  $Re$ ,  $Fr$ ,  $\tau$  and  $\omega$  are Reynold number, Froude number, shear  
 377 stress, stream power, respectively.  $^{**}$  refers to the significance of 0.01. The sample number is 90 for the fitted  
 378 equations.



379

380

**Figure 6** Runoff regime zones of upstream area and gully bed under different inflow discharge conditions.

381

### 3.1.3 Runoff shear stress and stream power of upstream area and gully bed

382

383

384

385

386

387

388

389

390

391

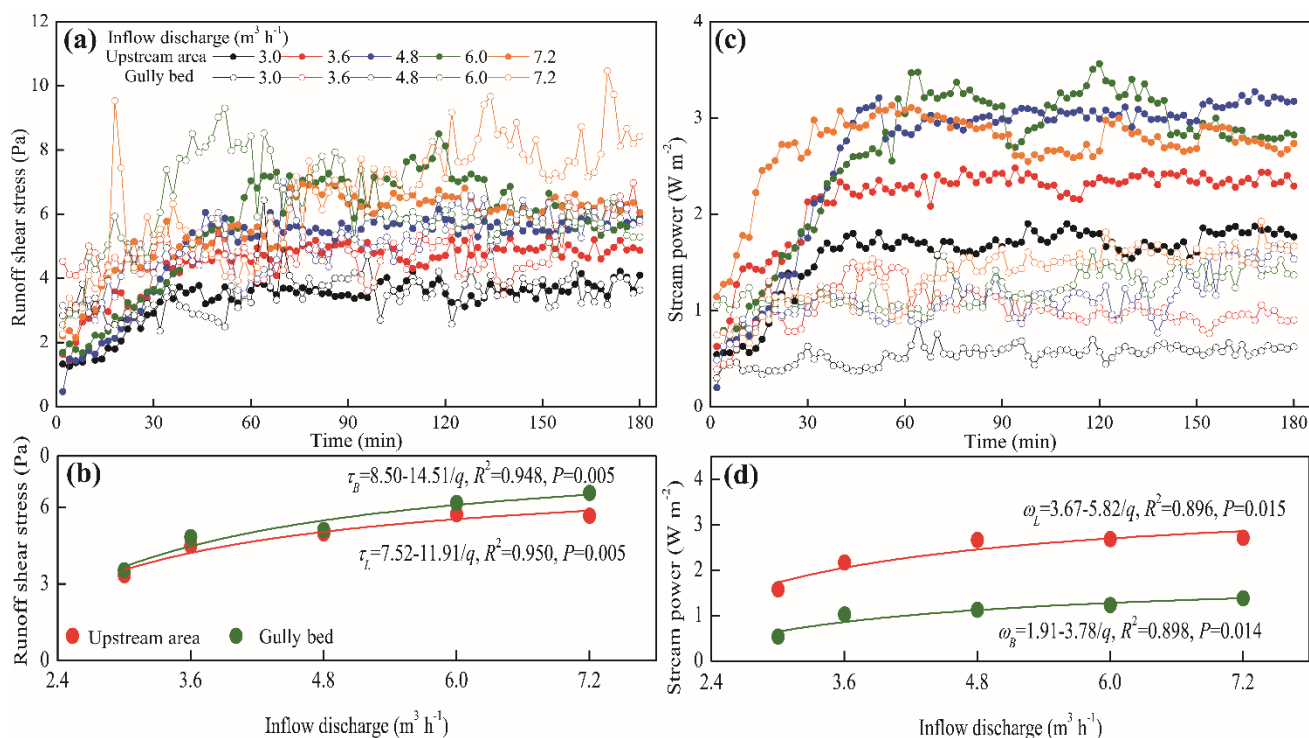
392

393

394

Fig.7 shows the temporal changes in runoff shear stress ( $\tau$ ) and stream power ( $\omega$ ) of upstream area (UA) and gully bed (GB) and their relationships with inflow discharge. Overall, the  $\tau$  of UA and GB exhibited a gradually increased trend in the first 60 min, and whereafter, a relative steady state was obtained, but the larger inflow discharge perturbed the steady situation (Fig. 7a). Furthermore, the temporal change in  $\tau$  of UA could be expressed by logarithmic functions, but the  $\tau$  of GB showed a significant power function with experimental time (Table 2). On average, the  $\tau$  of GB was 2.8% - 15.7% larger than the UA. The averaged  $\tau$  of UA and GB increased with inflow discharge as a power function ( $\tau=a-b/q$ ), and the GB had a faster increased-speed ( $b$ -value) than UA (Fig. 7b), signifying that the difference in  $\tau$  between UA and GB would be widened with the inflow discharge increased. Similarly, the  $\omega$  of UA and GB also exhibited a trend of gradual increase and stabilization (Fig. 7c). Different from the temporal change in  $\tau$ , the  $\omega$  of GB was always less than that of UA at any time for five inflow discharges. Likewise, the variation in  $\omega$  of UA and GB over time exhibited a significant logarithmic and power function, respectively. On average, the  $\omega$  of GB was 49.2% - 65.9% less than

395 UA, and the positive increase in  $\omega$  of UA and GB with inflow discharge could be expressed by a  
 396 power function (Fig. 7d).



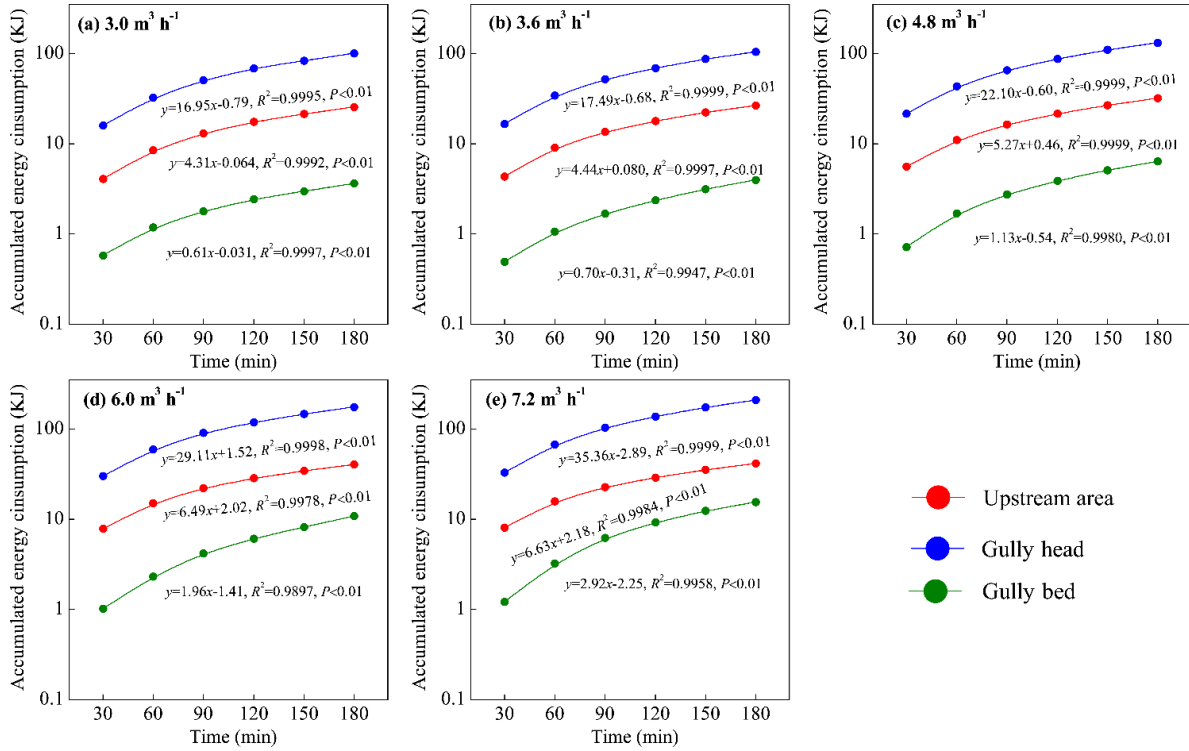
397  
 398 **Figure 7** Temporal changes in runoff shear stress and stream power of upstream area and gully bed and their  
 399 relationships with inflow discharge

### 400 3.2 Spatial-temporal change of energy consumption

401 Fig. 8 illustrates the temporal change in accumulated energy consumption of upstream area  
 402 (UA), gully head (GH) and gully bed (GB). The accumulated energy consumption of the three  
 403 landform units continued to linearly increase with time ( $R^2=0.990-0.999$ ,  $P<0.01$ ), of which the  
 404 accumulated energy consumption in GH was always the highest at any time, followed by UA and GB  
 405 under five inflow discharges. Moreover, the energy consumption rate (the slope-value of fitted  
 406 equation) in the three landform units is basically constant, indicating the spatial-temporal change in  
 407 energy consumption maintained a relatively steady state during gully headcut erosion. Moreover, the  
 408 energy consumption rate of GH was the highest, followed by UA and GB, and the energy  
 409 consumption rate in the three landform units also increased with the increase of inflow discharge.

410 The variations of total energy consumption of UA, GH and GB and their proportions with  
 411 inflow discharge are shown in Fig. 9. As illustrated in Fig. 9a, both of the total energy consumption  
 412 of the “UA-GH-GB” system and the three landform units increased with the increase of inflow

413 discharge. When inflow discharge increased from 3.0 to 7.2 m<sup>3</sup> h<sup>-1</sup>, the total energy consumption of  
414 the system, UA, GH and GB increased by 3.6% - 105.3%, 3.4% - 62.0%, 3.5% - 108.2% and 9.0% -  
415 327.5%, respectively. Regression analysis revealed that the energy consumption of the system and  
416 the three landform units increased with inflow discharge as an exponential function ( $y=a\cdot\exp(b\cdot x)$ ,  
417  $a=1.14 - 55.41$ ,  $b=0.13 - 0.36$ ,  $R^2=0.954 - 0.992$ ,  $P<0.05$ ). Furthermore, in view of the proportion of  
418 energy consumption, the energy consumption of UA accounted for 15.6% - 19.8% of total energy  
419 consumption, and linearly decreased with inflow discharge increased ( $R^2=0.933$ ,  $P<0.05$ ), whereas  
420 the proportion in GB (2.8% - 5.8%) linearly increased with inflow discharge increased ( $R^2=0.983$ ,  
421  $P<0.05$ ). However, the proportion of energy consumption (77.3% - 78.6%) in GH showed a weak  
422 change with inflow discharge (Fig. 9b), signifying that the most of runoff energy (77.5% on average)  
423 was consumed in the gully head position during headcut migration. Furthermore, we found that the  
424 total energy consumption (129.89 - 266.60 KJ) under different flow discharge conditions accounted  
425 for the 91.12% - 99.90% of total flow energy (Fig. 9c, 9d), which also indicated that only 0.10% -  
426 8.88% of total flow energy remained at the outlet of the “UA-GH-GB” system. These results fully  
427 implied that the most of flow energy (>91.12%) upstream from gully heads would be consumed  
428 during gully erosion, of which the gully headcut erosion (including plunge pool erosion) is the main  
429 process consuming flow energy.

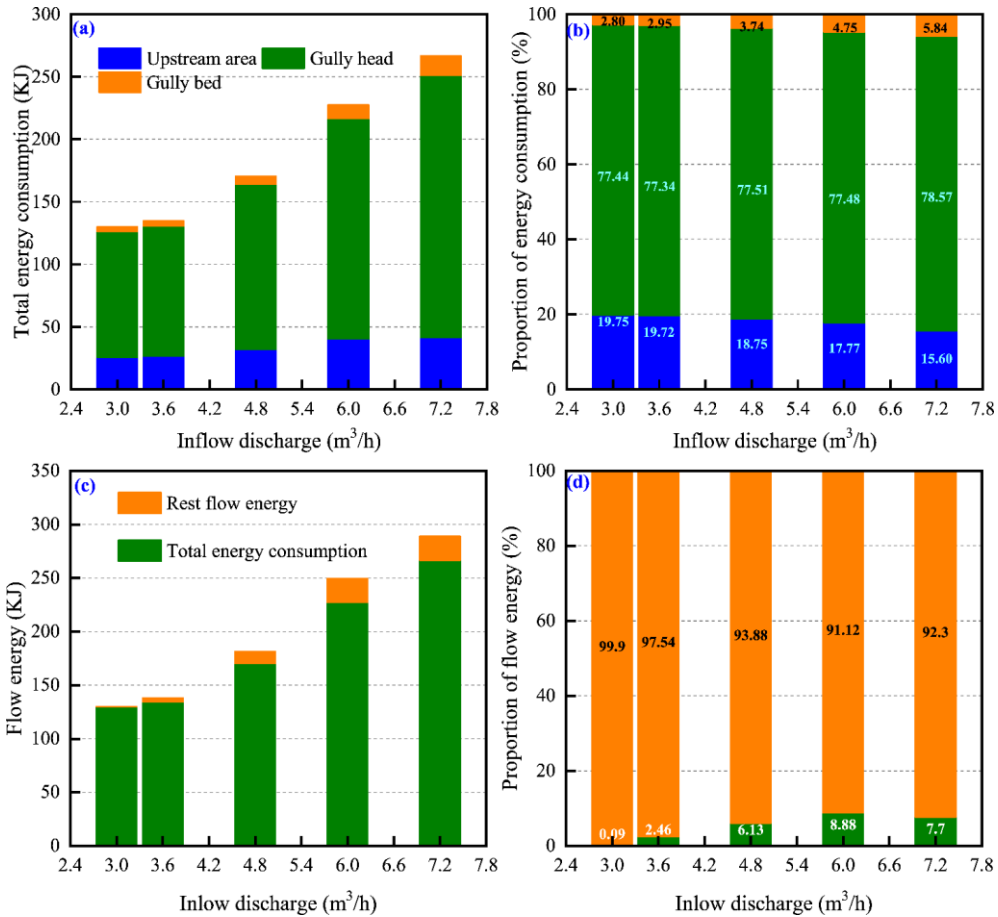


430

431

432

**Figure 8** Temporal changes in runoff energy consumption of upstream area, gully head and gully bed under different inflow discharge conditions



433

434

**Figure 9** The variation in energy consumption of upstream area, gully head and gully bed and their proportions

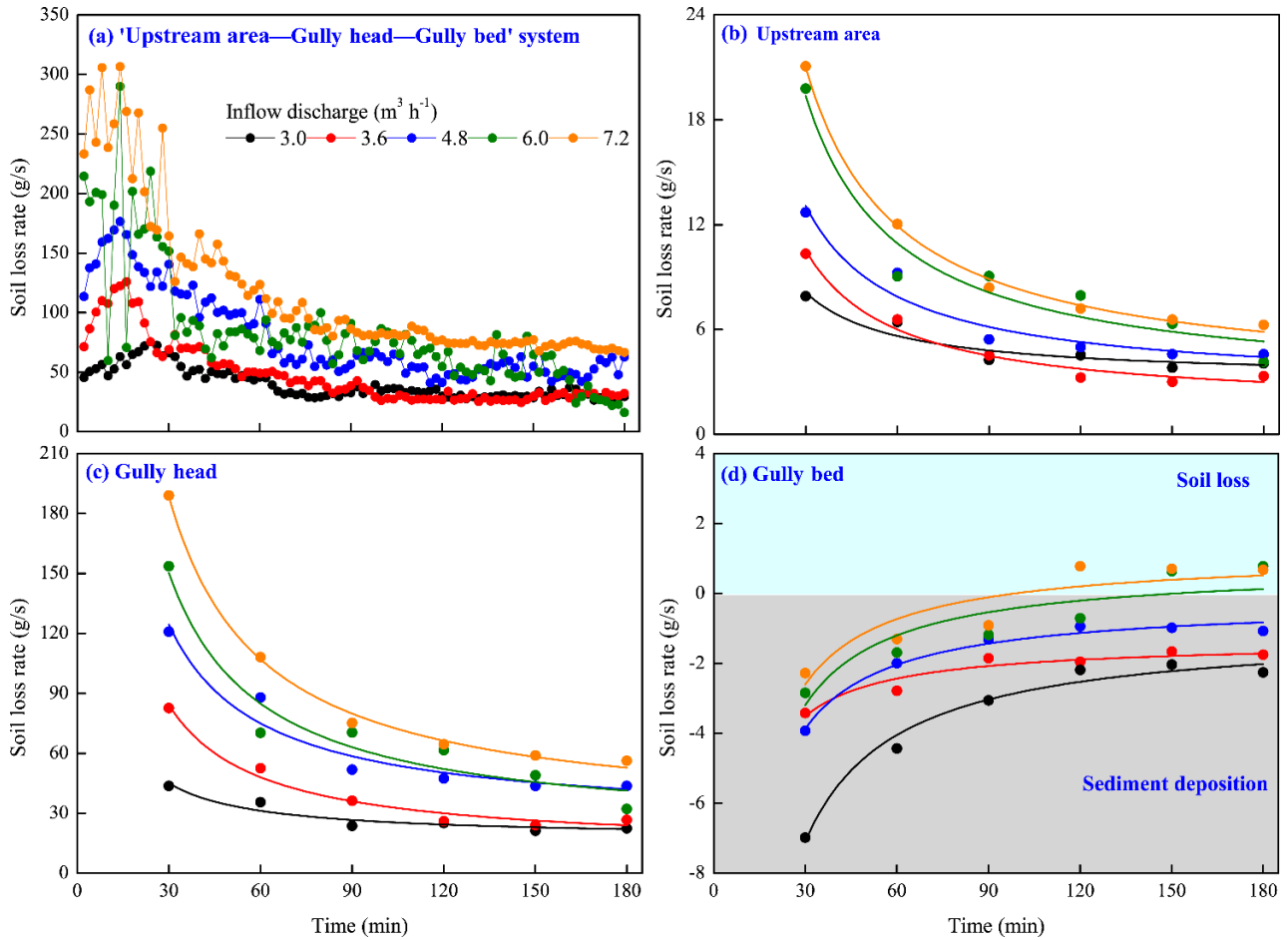
435

with inflow discharge

436 **3.3 Spatial-temporal change of soil loss**437 **3.3.1 Soil loss process**

438 Fig. 10a shows that the soil loss rate of the “upstream area (UA)—gully head (GH)—gully bed  
 439 (GB)” system rose to a peak in first 20 min, then gradually descend and levelled off. Especially for  
 440 the 6.0 and 7.2 m<sup>3</sup> h<sup>-1</sup>, the soil loss rate showed a severe fluctuation trend in the first 30 min. The  
 441 peak soil loss rate increased from 75.4 to 306.9 g s<sup>-1</sup> with increasing inflow discharge. The soil loss  
 442 of UA and GH experienced a similar change process. The soil loss rate was the highest in the early  
 443 stage of the experiment, and gradually decreased with time, and became stable after 120 min (Fig.  
 444 10b, 10c). Furthermore, the temporal variation in soil loss of UA and GH could be well expressed by  
 445 logarithmic function ( $S_L=a-b\cdot\ln(t)$ ,  $P<0.05$ , Table 3), and the  $a$ -value (representing initial soil loss  
 446 rate) and  $b$ -value (reflecting the reduction rate of soil loss rate with time) increased with increasing  
 447 inflow discharge, indicating that larger inflow discharge can improve initial soil loss of UA and GH  
 448 and also expedite the decrease of soil loss rate.

449 However, the GB presented a completely different soil loss process from UA and GH (Fig. 10d).  
 450 The GB was always characterized by sediment deposition during the whole experiment for the 3.0 –  
 451 4.8 m<sup>3</sup> h<sup>-1</sup> inflow discharges. The sediment deposition rate gradually decreased with time and  
 452 presented a significant “S” function over time ( $S_B=a/t-b$ ,  $R^2=0.918-0.982$ ,  $P<0.01$ , Table 3). When  
 453 the inflow discharge was larger than 4.8 m<sup>3</sup> h<sup>-1</sup>, the sediment generated from UA and GH was  
 454 deposited firstly in the GB and then gradually transported, and the temporal change of deposited  
 455 sediment on GB accorded with logarithmic functions ( $R^2=0.936$  and  $0.906$ ,  $P<0.01$ , Table 3).  
 456 Furthermore, two critical time points (135 min and 111 min) can be derived from the two fitted  
 457 logarithmic equations, which distinguished sediment deposition from sediment transport, signifying  
 458 that the runoff began to transport the deposited sediment on GB after 135 min and 111 min for 6.0  
 459 and 7.2 m<sup>3</sup> h<sup>-1</sup> inflow discharges.



460  
461  
462  
463

**Figure 10** Temporal variation in soil loss rate of the “upstream area—gully head—gully bed” system and each landform unit

**Table 3** Relationships between soil loss rate of three landform units and time

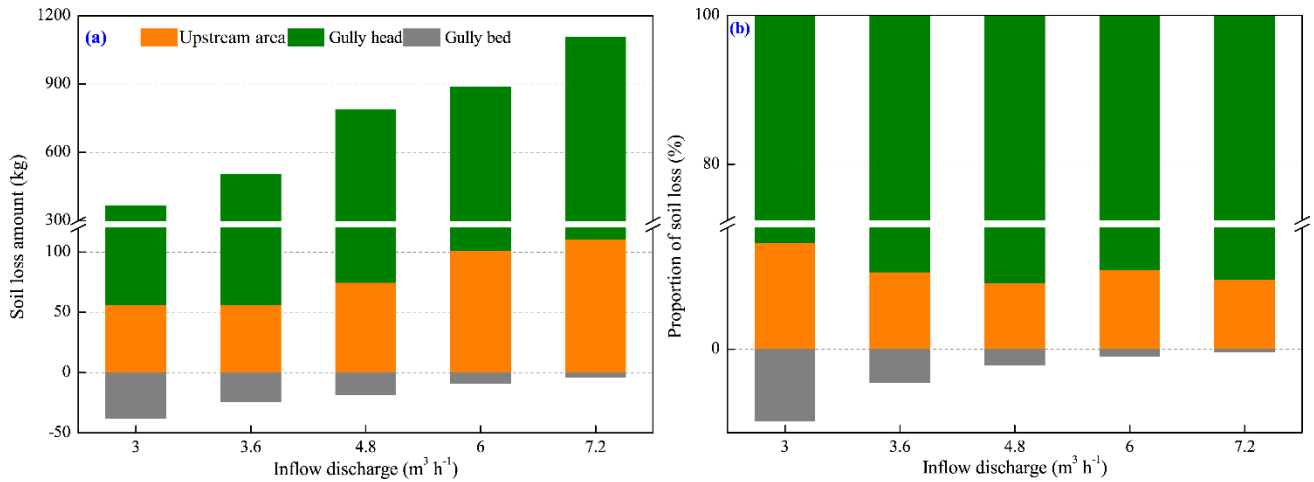
| Inflow discharge<br>(m <sup>3</sup> h <sup>-1</sup> ) | Fitted equations                          |   |  |
|---|---|---|--|
|   | Upstream area                             | Gully head                                  | Gully bed                                |
| 3.0   | $S_L=15.71-2.34\ln(t)$ , $R^2=0.909^{**}$ | $S_H=87.12-12.99\ln(t)$ , $R^2=0.908^{**}$  | $S_B=-182.62/t-1.01$ , $R^2=0.980^{**}$  |
| 3.6   | $S_L=23.97-4.18\ln(t)$ , $R^2=0.938^{**}$ | $S_H=191.82-33.44\ln(t)$ , $R^2=0.939^{**}$ | $S_B=-64.46/t-1.36$ , $R^2=0.918^{**}$   |
| 4.8   | $S_L=28.76-4.85\ln(t)$ , $R^2=0.930^{**}$ | $S_H=273.64-46.17\ln(t)$ , $R^2=0.929^{**}$ | $S_B=-109.36/t-0.22$ , $R^2=0.982^{**}$  |
| 6.0   | $S_L=44.0-7.69\ln(t)$ , $R^2=0.884^*$     | $S_H=341.59-59.74\ln(t)$ , $R^2=0.885^*$    | $S_B=2.03\ln(t)-9.96$ , $R^2=0.936^{**}$ |
| 7.2   | $S_L=47.34-8.25\ln(t)$ , $R^2=0.922^{**}$ | $S_H=425.24-74.07\ln(t)$ , $R^2=0.924^{**}$ | $S_B=1.86\ln(t)-8.76$ , $R^2=0.906^{**}$ |

464 Note:  $S_L$ ,  $S_H$  and  $S_B$  are the soil loss rate of upstream area, gully head and gully bed, respectively. The sample No. is  
465 6 for fitting equation. \* and \*\* indicate the significant level of 0.05 and 0.01.

### 466 3.3.2 Spatial distribution of soil loss

467 The variation in soil loss amount and proportion of the three landform units (UA, GH, GB) with  
468 inflow discharge is shown in Fig. 11. As illustrated in Fig. 11a, for the experiments of five inflow  
469 discharges, the soil loss was dominant in the UA and GH, but the GB was dominated by sediment  
470 deposition due to the weaker sediment transport capacity of runoff on GB than sediment

471 deliverability of UA and GH. Furthermore, the soil loss amount of UA and GH ranged from 55.9 to  
 472 110.7 kg and from 310.0 to 994.8 kg, respectively, and increased linearly with increasing inflow  
 473 discharge ( $R^2=0.966$  and  $0.969$ ,  $P<0.05$ ). The sediment deposition amount of GB ranged from 4.2 to  
 474 37.7 kg, and decreased with inflow discharge as a logarithmic function ( $R^2=0.961$ ,  $P<0.05$ ). In terms  
 475 of proportion of soil loss (Fig. 11b), the proportion of UA and GH reached the maximum (15.3%)  
 476 and minimum (84.7%), respectively under  $3.0 \text{ m}^3 \text{ h}^{-1}$  inflow discharge, whereas, the proportion  
 477 exhibited a little change (UA: 9.5% - 11.4%; GH: 88.6% - 90.5%) when the inflow discharge is  $7.2$   
 478  $\text{m}^3 \text{ h}^{-1}$ . Remarkably, the proportion of deposited sediment amount on GB to total soil loss amount  
 479 ranged from 0.4% to 10.3%, and decreased exponentially with inflow discharge ( $R^2=0.992$ ,  
 480  $P<0.001$ ).



481  
 482 **Figure 11** Variation in soil loss amount and proportion of upstream area, gully head and gully bed with inflow  
 483 discharge

### 484 3.4 Spatial change in hydrodynamic mechanism of soil loss

#### 485 3.4.1 Relationships between soil loss and hydraulic parameters

486 Fig. 12 indicates the significant difference in the relationships between soil loss rate and  
 487 hydraulic parameters among the three landform units (Fig. 12). For the upstream area (UA), the soil  
 488 loss rate could be described as a series of exponential functions of runoff velocity, Reynold number,  
 489 Froude number, runoff shear stress and stream power, of which the runoff shear stress and stream  
 490 power had a closer correlation with soil loss (Fig. 12a - 12e,  $R^2=0.830 - 0.945$ ). Furthermore, the  
 491 increased speed of soil loss rate obviously increased with the increasing hydraulic parameters (except  
 492 for runoff velocity), indicating that soil loss of UA showed a stronger sensitive response to increasing

493 hydraulic properties. However, the soil loss rate of gully bed (GB) linearly increased with the  
 494 above-mentioned five parameters (Fig. 12f – 12j,  $R^2=0.918 - 0.994$ ), which suggested that the  
 495 decreased rate of sediment deposition of GB is basically constant with the increasing hydraulic  
 496 properties. Further analysis showed that the critical runoff velocity, Reynold number, Froude number,  
 497 runoff shear stress and stream power for triggering the transformation of sediment deposition to soil  
 498 erosion on GB, and the critical values are  $0.26 \text{ m s}^{-1}$ , 2845, 0.85, 6.94 Pa and  $0.40 \text{ W m}^{-2}$ ,  
 499 respectively. For the gully head (GH) position, the soil loss was significantly affected by jet velocity  
 500 entry to plunge pool and jet shear stress (Fig. 12l and 12m,  $R^2=0.862$  and  $0.939$ ), while the  
 501 relationship between soil loss and flow velocity at the headcut brink-point was not significant (Fig.  
 502 12k,  $P=0.065$ ).

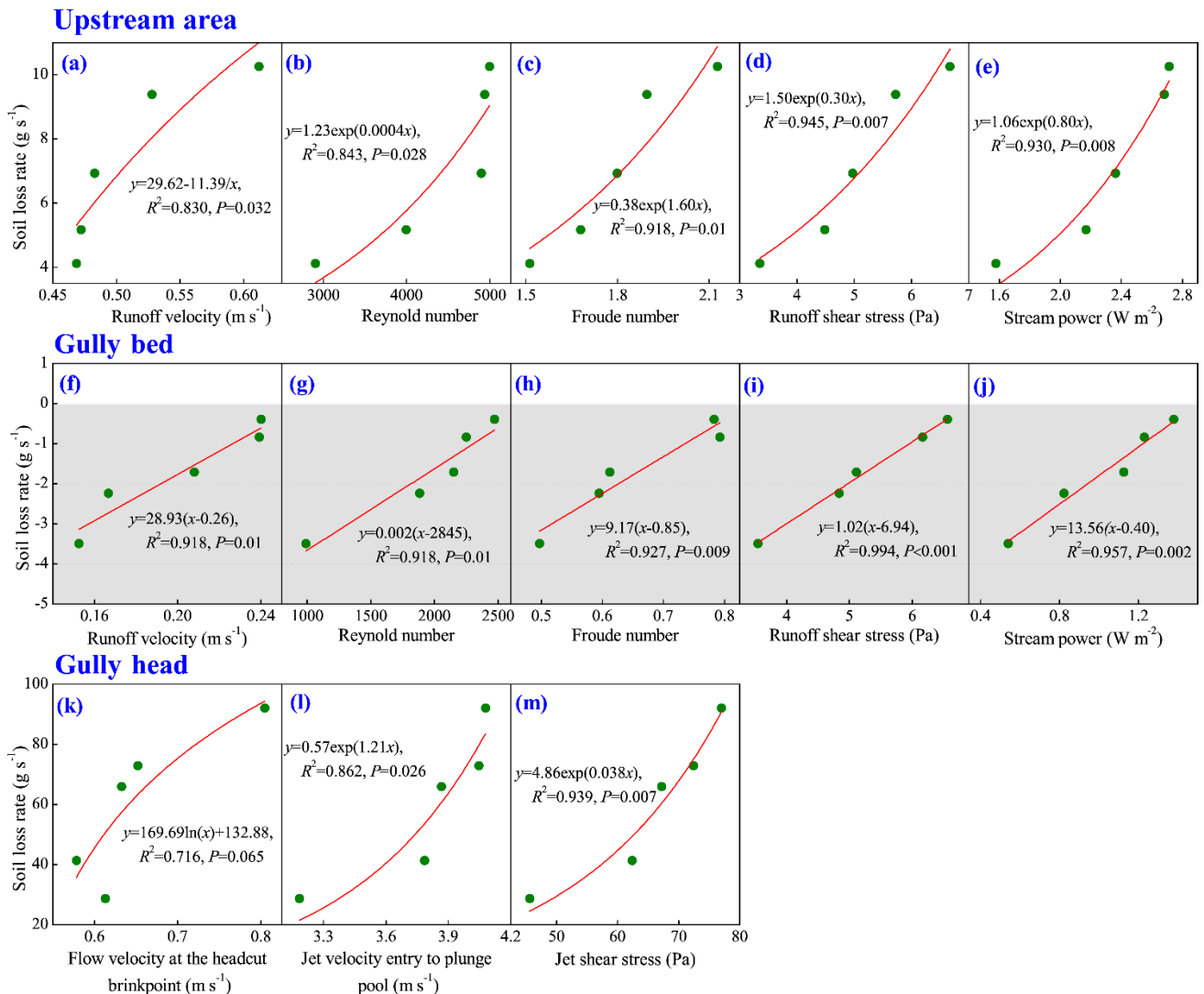


Figure 12 Relationships between soil loss rate of three landform units and hydraulic and jet properties

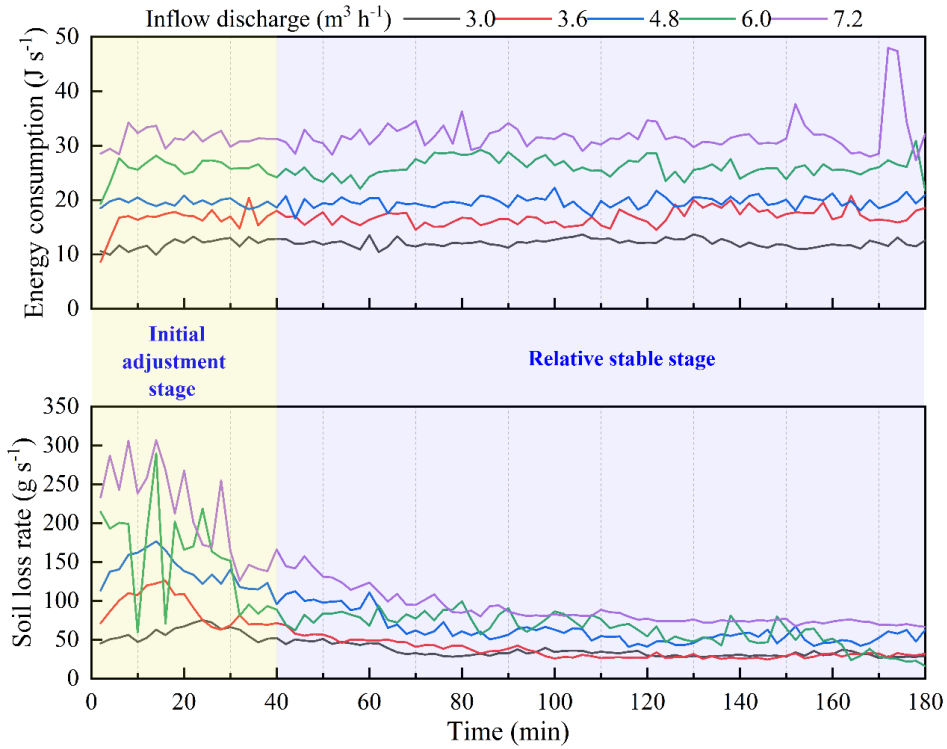
503  
 504  
 505



### 506 3.4.2 Response of soil loss to energy consumption

507 The synchronous change of soil loss of “UA-GH-GB” system and total energy consumption can  
508 be divided into two stages (Fig. 13). In the initial adjustment stage (0-40 min), the topsoil layer of  
509 UA had the relative higher erodibility and was the main resource of soil loss, which caused the  
510 relative lower flow velocity at the brinkpoint of gully head. Therefore, the most of flow discharge  
511 was transformed as on-wall flow, so the most of flow energy consumed at the headwall. So, in this  
512 stage, UA and gully headwall are the main positions of soil loss, and the most of flow energy was  
513 also consumed in the two positions. With the gradual adjustment of upstream area morphology, the  
514 gully erosion process entered into the relative stable stage (40-180 min). In this stage, the flow  
515 velocity at headcut obviously increased and showed a slight change (Fig. 4a), and thus the headwall  
516 erosion and plunge pool erosion also experienced a relative stable process. As a result, the soil loss  
517 and flow energy consumption exhibited a similar change process. Occasionally, the occurrence of  
518 several gully head and bank collapse events altered the synchronous change process of soil loss and  
519 energy consumption.

520 As illustrated in Fig. 14, on average, the soil loss rate of the “UA-GH-GB” system and the three  
521 individual landform units was positively and significantly related to the energy consumption  
522 ( $P < 0.05$ ), and a logarithmic function was found to fit the relationship between soil loss rate and  
523 energy consumption best ( $R^2 = 0.889 - 0.987$ ). The critical energy consumption initiating the system  
524 is  $7.53 \text{ J s}^{-1}$  (Fig. 14a). Furthermore, there is critical energy consumption to initiate soil erosion of the  
525 upstream area (UA) and gully head (GH) based on the fitted logarithmic functions (Fig. 14b, 14c).  
526 The critical energy consumption for GH ( $5.79 \text{ J s}^{-1}$ ) is 2.57 times greater than that ( $1.62 \text{ J s}^{-1}$ ) of the  
527 UA. Similarly, for the gully bed (Fig. 14d), the minimum energy consumption ( $1.64 \text{ J s}^{-1}$ ) is needed  
528 to trigger the transformation of sediment deposition to soil loss. We found that the sum of critical  
529 energy consumption initiating three landform units ( $9.05 \text{ J s}^{-1}$ ) was larger than the critical value  
530 initiating the system, which was mainly attributed to the mass failure of gully head and bank  
531 inputting the additional potential energy into the flow.

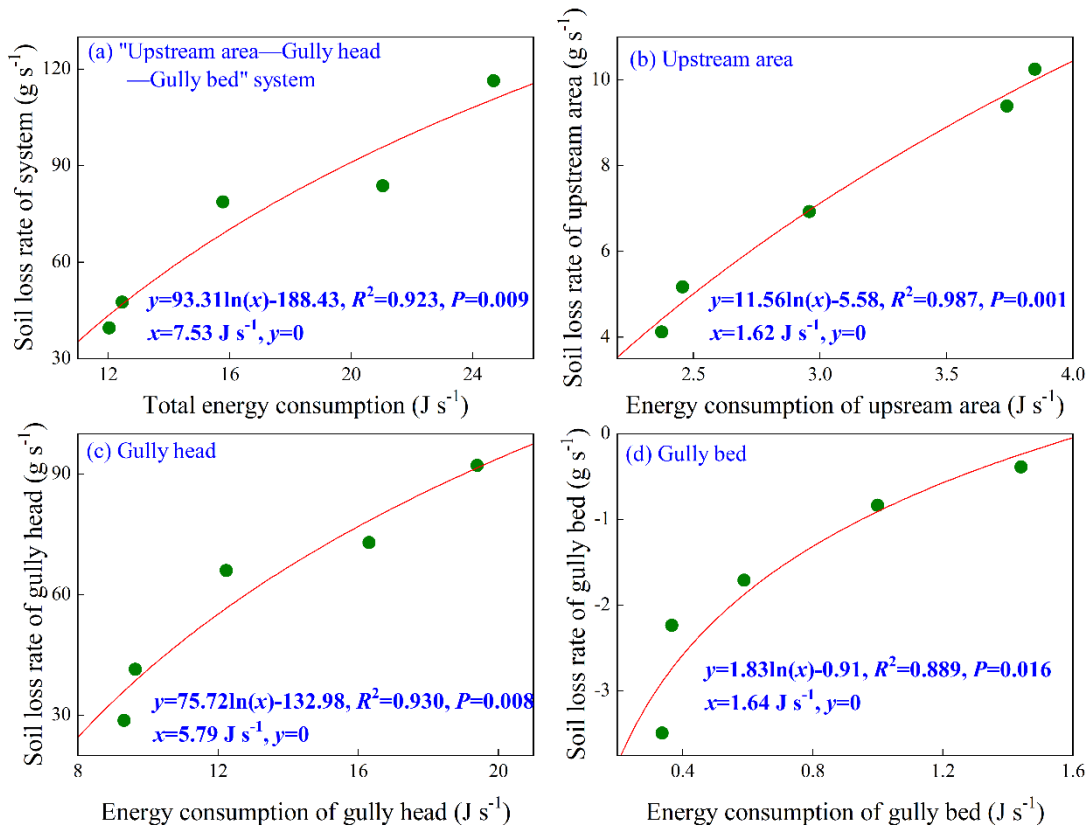


532

533

534

**Figure 13** Synchronous change of soil loss rate of “upstream area-gully head-gully bed” system and total energy dissipation during headcut erosion



535

536

537

**Figure 14** Relationships between soil loss rate of “upstream area-gully head-gully bed” system and three individual landform units and energy consumption

## 538 4 Discussion

### 539 4.1 Spatial-temporal changes in hydraulic properties

540 This study showed that the runoff velocity at the headcut brink-point ( $V_b$ ) firstly raised and then  
541 gradually stabilized with experimental duration (Fig. 4a), which was closely corresponded to the  
542 gradually decreased runoff width on the upstream area over time (Shi et al., 2020a). However, this  
543 result was inconsistent with Zhang et al (2016, 2018) and Shi et al (2020b) who reported that the  $V_b$   
544 decreased over time, which was mainly due to the gradually increased roughness and resistance of  
545 underlying surface over time reducing the runoff velocity in their studies (Battany and Grismer, 2015;  
546 Su et al., 2015). The further analysis of power function between  $V_b$  and time ( $V_b=a \cdot t^b$ , Table 1)  
547 showed that the  $a$ -value increased but the  $b$ -value showed a weak variation with the inflow discharge  
548 increased, indicating that upstream flow discharge can improve initial  $V_b$  but not affect its change  
549 trend over time. Therefore, we can extrapolate the erosion process and rule of upstream area from  
550 this simulation test to the actual ground situation. By contrast, the jet velocity entry to plunge pool  
551 ( $V_e$ ) and jet shear stress ( $\tau_j$ ) experienced a gradually decreased process (Fig. 4c, 4e), which was  
552 mainly attributed to the fact that the development of several second-headcut steps caused more  
553 energy consumption in plunge pools and the lower potential energy at headcut brink-point due to the  
554 shortened jet flow height (Guo et al., 2019; Jiang et al., 2020). This result, however, differed from the  
555 finding of Zhang et al. (2016) who stated the  $V_e$  and  $\tau_j$  remained stable as the experiments progressed,  
556 which was mainly attributed to the weak change of jet-flow height induced by slow headcut retreat.  
557 This comparison manifested that the jet flow properties was strongly determined by the headcut  
558 retreat process.

559 For the runoff hydraulic of upstream area (UA) and gully bed (GB), the Reynold number  $Re$  of  
560 UA and GB initially increased and gradually stabilized, but the Froude number  $Fr$  showed an  
561 opposite trend. This phenomenon was agreed with previous studies (e.g. Su et al., 2015; Zhang et al.,  
562 2016). Besides, the  $Re$  and  $Fr$  of UA were larger than that of GB by 50.5%-65.9% and 1.39-2.04  
563 times, respectively, under same inflow discharge upstream gully head, indicating that the runoff  
564 turbulence became weaker after the runoff of UA passed the gully head and experienced plunge pool  
565 erosion (Shi et al., 2020a). More evidently, the runoff on UA was in the supercritical-transition and

566 supercritical-turbulent flow regime ( $Re > 500$ ,  $Fr > 1$ ), whereas the runoff on GB belonged to  
567 subcritical-transition and subcritical-turbulent flow regime ( $Re > 500$ ,  $Fr < 1$ ). However, Su et al.  
568 (2015) found that the steady state  $Re$  of gully bed was higher than that of upstream area, which was  
569 mainly attributed to the difference in slope gradient. In their study, the larger gully bed slope gradient  
570 than upstream area would accelerate the runoff velocity and thus enhance flow turbulence (Bennett,  
571 1999; Pan et al., 2016). Furthermore, compared to UA, the  $\tau$  and  $\omega$  of GB increased and decreased  
572 by 2.8% - 15.7% and 49.2% - 65.9%, respectively. The increased shear stress was caused by the  
573 decrease of flow velocity on gully bed, and the drastically decreased stream power can reflect the  
574 energy consumption of flow for transporting sediment on gully bed. This result was different from  
575 some previous experimental studies on gully and bank gully under different conditions. Previous  
576 studies have proven that the lots of factors including plunge pool size, slope gradient, initial step  
577 height, and soil texture influenced the hydraulic properties from upstream area to gully bed is  
578 affected by various factors (Bennett and Casali, 2001; Wells et al., 2009a, 2009b).

#### 579 **4.2 Spatial-temporal change in runoff energy consumption and soil erosion**

580 Our study revealed that the accumulated runoff energy consumption of the upstream area (UA),  
581 gully headcut (GH) and gully bed (GB) linearly increased over time (Fig. 8), indicating the  
582 spatial-temporal change in energy consumption maintained a relatively steady state during gully  
583 headcut erosion. However, the flow energy consumption of bank gully in three landform units  
584 logarithmically increased over time (Su et al., 2015). This difference further manifested that the  
585 runoff energy consumption of different landform units depends on gully type to some extent as well  
586 as soil texture, slope and headwall height (Wells et al., 2009a). Besides, under this flow discharge  
587 conditions, the proportion of energy consumption to the total flow energy ranged from 91.12% to  
588 99.90%, indicating that almost all of flow energy was consumed during headcut erosion.  
589 Furthermore, the proportion of energy consumption in UA, GH and GB was 15.6%-19.8%,  
590 77.3%-78.6% and 2.8%-5.8%, respectively (Fig. 9), which was also indirectly supported by the study  
591 of Su et al. (2015) who suggested that the runoff energy consumption per unit soil loss from  
592 upstream area, headcut and gully bed is 17.4%, 70.5% and 12.0%, respectively. This further signified  
593 that the gully head consumed the most of runoff energy (77.5% on average) during headcut

594 migration. The flow energy must be consumed to surmount the soil resistance as headcut migrates,  
595 and the consumed energy was mainly focused on headwall and plunge pool development (Alonso et  
596 al., 2002).

597 In terms of soil loss, our study indicated that the soil loss rate of the “UA-GH-GB” system  
598 initially increased to the peak value and then gradually declined and stabilized (Fig. 10), which was  
599 consistent with the results of many studies on rill and gully headcut erosion under different  
600 conditions (slope, initial step height, flow discharge, soil type, soil stratification) (Bennett, 1999;  
601 Bennett and Casalí, 2001; Gordon et al., 2007; Wells et al., 2009a; Shi et al., 2020a). Both the scour  
602 depth and sediment production increased in the initial period of underlying surface adjustment, while  
603 once the plunge pool development was maintained, and sediment yield decreased and gradually  
604 stabilized (Bennett et al., 2000). In addition, the significant difference in soil loss process was found  
605 among the three landform units. The soil loss of UA and GH decreased logarithmically over time,  
606 which was similar with several studies (e.g., Su et al., 2015; Shi et al., 2020b). Nevertheless, the GB  
607 was always characterized by sediment deposition for the inflow discharge of  $< 4.8 \text{ m}^3 \text{ h}^{-1}$ , whereas  
608 the sediment was deposited firstly and then gradually transported as the inflow discharge increased to  
609  $6.0$  and  $7.2 \text{ m}^3 \text{ h}^{-1}$ . Similar phenomena was also found in some previous studies on rill heacut erosion  
610 (Bennett, 1999; Bennett and Casalí, 2001; Gordon et al., 2007; Wells et al., 2009a). This further  
611 indicated that soil loss/deposition process of gully system was significantly influenced by three  
612 landform units, and especially, the most of flow energy (77.5%) consumed at gully heads due to jet  
613 flow erosion strongly weakened sediment transport capacity of flow on gully bed and thus changed  
614 the soil loss/deposition process of gully system. However, Su et al. (2014, 2015) revealed a larger  
615 soil loss volume or soil loss rate in gully bed than upstream area and headwall during bank gully  
616 headcut erosion. This difference between our study and Su et al. (2014, 2015) is primarily caused by  
617 the difference in slope gradient. The gully bed slope ( $20^\circ$ ) of bank gully was larger than that ( $3^\circ$ ) of  
618 our study, indicating the runoff on gully bed of bank gully had stronger sediment transport capacity  
619 (Zhang et al., 2009; Ali et a., 2013; Wu et al., 2016, 2018). Besides, some previous also proved that  
620 the soil type, surface roughness, slope-length, groundwater/surface runoff were the main factors  
621 influencing soil loss by gully erosion (Amare et al., 2020; Li et al., 2021). In view of the proportion

622 of soil loss, the proportion of UA and GH was 9.5% - 11.4% and 88.6% - 90.5%, respectively, of  
623 which the proportion of deposited sediment on GB to the sediment yield from UA and GH can reach  
624 up to 0.4% - 10.3%. This result fully demonstrated that the gully head is the main source of sediment  
625 production during gully headcut erosion (Oostwoud-Wijdenes & Bryan, 1994; Zhao, 1994; Su et al.,  
626 2014), and also manifested the necessary and importance of gully headcut erosion controlling in  
627 gully-dominated region (Amare et al., 2019).

### 628 **4.3 Hydrodynamic characteristics of headcut erosion**

629 The significantly different relationships between soil loss and jet or hydraulic characteristics  
630 were found among UA, GH, and GB. The soil loss rate of UA exponentially increased with five  
631 hydraulic parameters (runoff velocity, Reynold number, Froude number, runoff shear stress and  
632 stream power), indicating that soil loss of UA showed a stronger sensitive response to increasing  
633 hydraulic properties. This could attribute to the frequent bank collapse on UA accelerating soil loss  
634 (Wells et al., 2013; Qin et al., 2018). However, the sediment deposition rate of GB linearly decreased  
635 with the five hydraulic parameters, signifying that sediment deposition on GB decreased at a stable  
636 state with the increase of hydraulic parameters. Therefore, the sediment deposition rate would reach  
637 zero when the five hydraulic parameters increased to the critical values, implying that the  
638 transformation of sediment deposition to sediment transport on GB would be triggered. Furthermore,  
639 the shear stress is the optimal parameter describing soil loss process of UA and GB, which differed  
640 from some studies on hillslope/gully erosion hydrodynamic characteristics (Zhang et al., 2009; Shen  
641 et al., 2019; Ma et al., 2020; Sidorchuk, 2020). Most of studies have verified that stream power is the  
642 superior hydrodynamic parameter describing soil detachment process. This comparison also fully  
643 illustrated the great difference in hydrodynamic characteristic between hillslope erosion and headcut  
644 erosion. In this study, the soil loss of gully head (including plunge pool erosion) was significantly  
645 affected by jet properties. It's confirmed that the plunge pool erosion by jet flow becomes a crucial  
646 process controlling gully head migration and sediment production (Oostwoud-Wijdenes et al., 2000).  
647 Consequently, the plunge pool erosion theory is usually employed to build several headcut retreat  
648 models (Alonso et al., 2002; Campo-Bescós et al., 2013). Although the weak correlation between soil  
649 loss of gully head and flow velocity at headcut breakpoint, the larger flow velocity resulted from

650 increasing inflow discharge would improve the shear stress of jet flow impinging gully bed, and thus  
651 the gully headcut suffered stronger incisional erosion of the plunge pool. However, in fact, the soil  
652 loss of gully head was also affected by on-wall flow erosion (Chen et al., 2013; Guo et al., 2021a),  
653 and thus more studies should be conducted to clear the effect of on-wall flow properties on headwall  
654 erosion.

655 From the energy consumption perspective, the soil loss rate of the three landform units  
656 significantly and logarithmically increased with the energy consumption, and the similar change  
657 trend was also found in the study of Su et al. (2015). This finding suggests that energy consumption  
658 could be considered as the available parameter to estimate the soil loss of gully headcut erosion (Shi  
659 et al., 2020b). Furthermore, we found the critical energy consumption initiating soil erosion of UA,  
660 GH, and GB are  $1.62 \text{ J s}^{-1}$ ,  $5.79 \text{ J s}^{-1}$  and  $1.64 \text{ J s}^{-1}$ , respectively, indicating the soil loss of gully head  
661 (including plunge pool) needs more flow energy consumption (Zhang et al., 2018; Shi et al., 2020a,  
662 2020b). This phenomenon can be attributed to the fact that the more runoff energy was consumed at  
663 the gully headwall and plunge pool erosion than UA and GB and thus resulted in more severe soil  
664 loss during headcut erosion. In addition, we found that the critical energy consumption activating soil  
665 loss of “UA-GH-GB” system was lower the sum of critical energy consumption initiating soil loss  
666 and sediment transport of three landform units ( $9.05 \text{ J s}^{-1}$ ). This result was closely related to mass  
667 failures such as gully head and gully bank collapse can contribute the additional energy into the flow.  
668 So, the role of gravitational erosion in controlling gully erosion process should be clarified in the  
669 future studies.

## 670 **5 Implication, significance and limitations of this study**

671 Gully erosion has been studied for nearly a century, but its process and dynamic mechanism are  
672 still difficult to clearly understand and reveal. Given this, our study attempted to clarify the  
673 spatial-temporal changes in flow hydraulic characteristics, energy consumption and soil loss and  
674 expound the response of soil loss to runoff properties and energy consumption during headcut  
675 erosion through a series of simulation experiment under controlled conditions. These results could be  
676 extended to wider conditions, such as gully scale, flow discharge determined by rainfall and drainage  
677 area, which can promote the understanding of process and mechanism of gully erosion under real

678 ground conditions as well as the modelling and prediction of gully erosion. Especially, the variation  
679 and proportion of energy consumption along “UA-GH-GB” in the process of gully erosion and its  
680 influence on sediment yield were clearly elucidated in this study, which has an important guiding  
681 significance for gully erosion control practice and restoration efforts. We can design some  
682 engineering and/or vegetation measures at gully heads to pre-consume the most flow energy and the  
683 energy dissipation structures could be designed and installed at the position where plunge pool  
684 develops. Also, the appropriate size of these measures also can be determined to ensure the flow  
685 energy of different landform units was lower than the corresponding critical energy consumption.

686 However, there are some potential limitations in our study. First, considering the complex  
687 effects of lots of factors on gully erosion, the flow discharge upstream gully heads was designed as  
688 the core factor affecting gully erosion in our study, and the five levels of flow discharge was  
689 generated according to the rainfall, landform and gully morphology. But it is not really same as the  
690 actual ground situations, such as the flow discharge upstream gully heads would not be constant  
691 during a rainfall event. Second, it has not been confirmed how well our experimental results are in  
692 line with the actual ground results. Therefore, further studies need to verify the experimental results  
693 with the actual situations, so that the study results can be practiced and applied under actual rainfall  
694 conditions. Third, in the future research, gully erosion experiments under different control measures  
695 should be carried out to identify suitable gully erosion prevention measures. Although the  
696 earlier-noted imperfection represents the limitation of our study, we still clearly demonstrated the  
697 temporal-spatial change in hydraulic properties and soil loss during headcut erosion and quantify the  
698 response relationships of soil loss of different landform units to energy consumption, which is of  
699 great significance for deepening the understanding of the gully process and hydrodynamic  
700 mechanism. Also, our results can provide valuable ideas and scientific basis for the construction of  
701 gully erosion model and the design of gully erosion prevention measures.

## 702 **Summary**

703 This study investigated the temporal-spatial changes in flow hydraulic, energy consumption and  
704 soil loss during headcut erosion based on a series of scouring experiments of gully headcut erosion.  
705 The jet properties of gully head (GH) were significantly affected by upstream inflow discharge. The



706 upstream area (UA) and gully bed (GB) had similar temporal changes in Reynold number, Froude  
707 number, shear stress and stream power. The flow was supercritical on UA, but subcritical on GB, and  
708 the turbulent degree was enhanced by the increasing inflow discharge. The flow Reynold number,  
709 shear stress and stream power decreased by 56.0%, 63.8% and 55.9%, respectively, but Froude  
710 number increased by 7.9% when flow passed the gully headcut and plunge pool. The accumulated  
711 energy consumption at UA, GH and GB linearly increased with time. Overall, 91.12% - 99.90% of  
712 total flow energy was consumed during headcut erosion, of which the GH accounted for 77.5% of  
713 the total runoff energy dissipation followed by UA (18.3%) and GB (4.0%). The soil loss of UA and  
714 GH decreased logarithmically over time, whereas the GB was mainly characterized by sediment  
715 deposition. The GH and UA contributed 88.5% and 11.5% of total soil loss, respectively, of which  
716 3.8% sediment production was deposited on GB. The soil loss of UA and GH and the sediment  
717 deposition of GB were significantly affected by hydraulic and jet properties. Our study revealed that  
718 the critical energy consumption to initiate soil erosion of UA, GH and GB are  $1.62 \text{ J s}^{-1}$ ,  $5.79 \text{ J s}^{-1}$   
719 and  $1.64 \text{ J s}^{-1}$ , respectively. The runoff energy consumption could be considered as a non-negligible  
720 parameter to predict gully headcut erosion.

## 721 **Data availability**

722 At present, the original data are not publicly accessible because of a situation that we don't have  
723 permission to share data according to the requirement of the funded program and our institute.  
724 However, we are pleasure to share all data plotted in figures in this study for other colleagues.

## 725 **Author contribution**

726 Mingming Guo and Wenlong Wang designed the experiments. Mingming Guo, Zhuoxin Chen,  
727 Tianchao Wang, Qianhua Shi, Man Zhao and Lanqian Feng carried out the experiments. Zhuoxin  
728 Chen produced and processed the digital elevation model of erosion landform. Mingming Guo and  
729 Wennlong Wang written and prepared the manuscript with contributions from all co-authors.

## 730 **Competing interests:**

731 The authors declare that they have no conflict of interest.

732 **Acknowledgments**

733 This work was supported by the National Natural Science Foundation of China (42077079,  
734 41571275), the China Postdoctoral Science Foundation (2020M681062), and the National Key  
735 Research and Development Program of China (2016YFC0501604). Acknowledgement for the data  
736 support from "Loess Plateau Data Center, National Earth System Science Data Sharing Infrastructure,  
737 National Science & Technology Infrastructure of China. (<http://loess.geodata.cn>)".

738 **References**

- 739 Addisie, M.B., Ayele, G.K., Gessess, A.A., Tilahun, S.A., Zegeye, A.D., Moges, M.M., ... Steenhuis, T.S.:  
740 Gully head retreat in the sub-humid Ethiopian Highlands: The Ene-Chilala catchment, *Land Degradation &*  
741 *Development*, 28, 1579–1588, <https://doi.org/10.1002/ldr.2688>, 2017.
- 742 Ali, M., Seeger, M., Sterk, G., Moore, D.: A unit stream power based sediment transport function for overland  
743 flow. *Catena*. 101, 197-204. <https://doi.org/10.1016/j.catena.2012.09.006>
- 744 Alonso, C.V., Bennett, S.J., Stein, O.R., 2002. Predicting head cut erosion and migration in concentrated flows  
745 typical of upland areas, *Water Resources Research*, 38, 39-1–39-15, <http://dx.doi.org/10.1029/2001WR001173>,  
746 2013.
- 747 Amare, S., Keesstra, S., van der Ploeg, M., Langendoen, E., Steenhuis, T., Tilahun, S.: Causes and controlling  
748 factors of Valley bottom Gullies. *Land*, 8(9), 141, <https://doi.org/10.3390/land8090141>, 2019.
- 749 Amare, S., Langendoen, E., Keesstra, S., Ploeg, M. V. D., Gelagay, H., Lemma, H., van der Zee, S. E.:  
750 Susceptibility to Gully Erosion: Applying Random Forest (RF) and Frequency Ratio (FR) Approaches to a  
751 Small Catchment in Ethiopia. *Water*, 13(2), 216, <https://doi.org/10.3390/w13020216>, 2021.
- 752 Arabameri, A., Chen, W., Lombardo, L., Blaschke, T., Tien Bui, D.: Hybrid computational intelligence models  
753 for improvement gully erosion assessment, *Remote Sensing*, 12(12), <https://doi.org/10.3390/rs12010140>, 140,  
754 2020.
- 755 Battany, M.C., Grismer, M.E.: Rainfall runoff and erosion in Napa Valley vineyards: effects of slope, cover  
756 and surface roughness, *Hydrological Processes*, 14(7), 1289-1304,  
757 [https://doi.org/10.1002/\(SICI\)1099-1085\(200005\)14:7<1289::AID-HYP43>3.0.CO;2-R](https://doi.org/10.1002/(SICI)1099-1085(200005)14:7<1289::AID-HYP43>3.0.CO;2-R), 2015.
- 758 Beer, C.E., Johnson, H.P.: Factors in gully growth in the deep loess area of western Iowa. *Transactions of*  
759 *ASAE*, 6, 237–240, <https://doi.org/10.13031/2013.40877>, 1963.
- 760 Belayneh, M., Yirgu, T., Tsegaye, D.: Current extent, temporal trends, and rates of gully erosion in the Gumara  
761 watershed, northwestern Ethiopia, *Global Ecology and Conservation*, 24, e01255,  
762 <https://doi.org/10.1016/j.gecco.2020.e01255>, 2020.
- 763 Bennett, S.J., Casali, J.: Effect of initial step height on headcut development in upland concentrated flows.  
764 *Water Resources Research*, 37, 1475–1484, <https://doi.org/10.1029/2000WR900373>, 2001.
- 765 Bennett, S.J.: Effect of slope on the growth and migration of headcuts in rills, *Geomorphology*, 30, 273–290,  
766 [https://doi.org/10.1016/S0169-555X\(99\)00035-5](https://doi.org/10.1016/S0169-555X(99)00035-5), 1999.
- 767 Bennett, S.J., Alonso, C.V.: Turbulent flow and bed pressure within headcut scour holes due to plane  
768 reattached jets, *Journal of Hydraulic Research*, 44, 510–521, <https://doi.org/10.1080/00221686.2006.9521702>,  
769 2006.

770 Bennett, S.J., Alonso, C.V., Prasad, S.N., Romkens, M.J.: Experiments on headcut growth and migration in  
771 concentrated flows typical of upland areas, *Water Resources Research*, 36, 1911–1922,  
772 <https://doi.org/10.1029/2000WR900067>, 2000.

773 Bogale, A. G., Aynalem, D. W., Adem, A. A., Mekuria, W., Tilahun, S.: Spatial and temporal variability of soil  
774 loss in gully erosion in upper Blue Nile basin, Ethiopia, *Applied Water Science*, 10(5), 106,  
775 <https://doi.org/10.1007/s13201-020-01193-4>, 2020.

776 Campo-Bescós, M.A., Flores-Cervantes, J.H., Bras, R.L., Casalí, J., Giráldez, J.V.: Evaluation of a gully  
777 headcut retreat model using multitemporal aerial photographs and digital elevation models, *Journal of*  
778 *Geophysical Research: Earth Surface*, 118, 2159–2173, <https://doi.org/10.1002/jgrf.20147>, 2013.

779 Chaplot, V., Giboire, G., Marchand, P., Valentin, C.: Dynamic modelling for linear erosion initiation and  
780 development under climate and land-use changes in northern Laos, *Catena*, 63, 318–328,  
781 <https://doi.org/10.1016/j.catena.2005.06.008>, 2005.

782 Che, X.L.: Study of distribution characteristic and evolution of headward erosion on Dongzhi tableland of the  
783 loess gully region, Yangling: Northwest A&F University, pp. 66-67, (In Chinese), 2012.

784 Chen, A., Zhang, D., Peng, H., Fan, J., Xiong, D., Liu, G.: Experimental study on the development of collapse  
785 of overhanging layers of gully in Yuanmou Valley, China, *Catena*, 109, 177-185,  
786 <https://doi.org/10.1016/j.catena.2013.04.002>, 2013.

787 De Baets, S., Poesen, J., Knapen, A., Galindo, P.: Impact of root architecture on the erosion-reducing potential  
788 of roots during concentrated flow, *Earth Surface Processes and Landforms*, 32, 1323–1345,  
789 <https://doi.org/10.1002/esp.1470>, 2007.

790 de Vente, J., Poesen, J.: Predicting soil erosion and sediment yield at the basin scale: Scale issues and  
791 semi-quantitative models, *Earth-Science Reviews*, 71, 95–125, <https://doi.org/10.1016/j.earscirev.2005.02.002>,  
792 2005.

793 DeLong, S.B., Johnson, J., Whipple, K.: Arroyo channel head evolution in a flash-flood-dominated  
794 discontinuous ephemeral stream system, *Geological Society of America Bulletin*, 126, 1683–1701,  
795 <https://doi.org/10.1130/B31064.1>, 2014.

796 Descroix, L., González Barrios, J.L., Viramontes, D., Poulenard, J., Anaya, E., Esteves, M., Estrada, J.: Gully  
797 and sheet erosion on subtropical mountain slopes: their respective roles and the scale effect, *Catena*, 72, 325–  
798 339, <https://doi.org/10.1016/j.catena.2007.07.003>, 2008.

799 Dotterweich, M., Rodzik, J., Zglobicki, W., Schmitt, A., Schmidtchen, G., Bork, H.R.: High resolution gully  
800 erosion and sedimentation processes, and land use changes since the Bronze Age and future trajectories in the  
801 Kazimierz Dolny area (Nałęczów Plateau, SE-Poland), *Catena*, 95, 50–62,  
802 <https://doi.org/10.1016/j.catena.2012.03.001>, 2012.

803 Flores-Cervantes, J., Istanbuluoglu, E., Bras, R.: Development of gullies on the landscape: A model of  
804 headcut retreat resuUAing from plunge pool erosion, *Journal of Geophysical Research*, 111, 1–14,  
805 <https://doi.org/10.1029/2004JF000226>, 2006.

806 Frankl, A., Stal, C., Abraha, A., Nyssen, J., Rieke-Zapp, D., DeWulf, A., Poesen, J.: Detailed recording of  
807 gully morphology in 3D through image-based modelling, *Catena*, 127, 92–101,  
808 <https://doi.org/10.1016/j.catena.2014.12.016>, 2015.

809 Fu, B.J., Liu, Y., Lv, Y.H., He, C.S., Zeng, Y., Wu, B.F.: Assessing the soil erosion control service of  
810 ecosystems change in the Loess Plateau of China, *Ecological Complexity*, 8, 284-293,  
811 <https://doi.org/10.1016/j.ecocom.2011.07.003>, 2011.

812 Gordon, L.M., Bennett, S.J., Wells, R.R., Alonso, C.V.: Effect of soil stratification on the development and  
813 migration of headcuts in upland concentrated flows, *Water Resources Research*, 43, W07412,  
814 <https://doi.org/10.1029/2006WR005659>, 2007.

815 Guo, M., Wang, W., Shi, Q., Chen, T., Kang, H., Li, J.: An experimental study on the effects of grass root  
816 density on gully headcut erosion in the gully region of China's Loess Plateau, *Land Degradation &  
817 Development*, 30, 2107–2125, <https://doi.org/10.1002/ldr.3404>, 2019.

818 Guo, M., Wang, W., Wang, T., Wang, W., Kang, H.: Impacts of different vegetation restoration options on  
819 gully head soil resistance and soil erosion in loess tablelands, *Earth Surface Processes and Landforms*, 45(4),  
820 1038-1050, <https://doi.org/10.1002/esp.4798>, 2020a.

821 Guo, M.M., Wang, W.L., Kang, H.L., Yang, B.: Changes in soil properties and erodibility of gully heads  
822 induced by vegetation restoration on the Loess Plateau, China, *Journal of Arid Land*, 10(5), 712-725,  
823 <https://doi.org/10.1007/s40333-018-0121-z>, 2018.

824 Guo, M.M., Wang, W.L., Li, J.M., Bai, Y., Kang, H.L., Yang, B.: Runoff characteristics and soil erosion  
825 dynamic processes on four typical engineered landforms of coalfields: An in-situ simulated rainfall  
826 experimental study, *Geomorphology*, 349, 106896, <https://doi.org/10.1016/j.geomorph.2019.106896>, 2020b.

827 Guo, M.M., Lou, Y.B., Chen, Z.X., Wang, W.L., Feng, L.Q., Zhang, X.Y.: The proportion of jet flow and  
828 on-wall flow and its effects on soil loss and plunge pool morphology during gully headcut erosion, *Journal of  
829 Hydrology*, 598, 126220, <https://doi.org/10.1016/j.jhydrol.2021.126220>, 2021a.

830 Guo, M.M., Chen, Z.X., Wang, W.L., Wang, T.C., Wang, W.X., Cui, Z.Q.: Revegetation induced change in  
831 soil erodibility as influenced by slope situation on the Loess Plateau, *Science of the Total Environment*, 772,  
832 145540, <https://doi.org/10.1016/j.scitotenv.2021.145540>, 2021b.

833 Hager, W.H.: Hydraulics of plane free overfall, *Journal of Hydraulic Engineering*, 109, 1683–1697,  
834 [https://doi.org/10.1061/\(ASCE\)0733-9429\(1983\)109:12\(1683\)](https://doi.org/10.1061/(ASCE)0733-9429(1983)109:12(1683)), 1983.

835 Hanson, G.J., Robinson, K.M., Cook, K.R.: Prediction of headcut migration using a deterministic approach,  
836 *Transactions of the ASAE*, 44(4), 525-531, <https://doi.org/10.13031/2013.6112>, 2001.

837 Hosseinalizadeh, M., Kariminejad, N., Chen, W., Pourghasemi, H.R., Alinejad, M., Behbahani, A.M.,  
838 Tiefenbacher, J.P.: Gully headcut susceptibility modeling using functional trees, naïve Bayes tree, and random  
839 forest models, *Geoderma*, 342, 1-11, <https://doi.org/10.1016/j.geoderma.2019.01.050>, 2019.

840 Ionita, I.: Gully development in the Moldavian Plateau of Romania, *Catena*, 68, 133–140,  
841 <https://doi.org/10.1016/j.catena.2006.04.008>, 2006.

842 Ionita, I., Niacsu, L., Petrovici, G., Blebea-Apostu, A.M.: Gully development in eastern Romania: a case study  
843 from Falciu Hills, *Natural Hazards*, 79, 113–138, <https://doi.org/10.1007/s11069-015-1732-8>, 2015.

844 Jiang, Y., Shi, H., Wen, Z., Guo, M., Zhao, J., Cao, X., Fan, Y., Zheng, C.: The dynamic process of slope rill  
845 erosion analyzed with a digital close range photogrammetry observation system under laboratory conditions,  
846 *Geomorphology*, 350, 106893, <https://doi.org/10.1016/j.geomorph.2019.106893>, 2020.

847 Jiao, J.Y., Wang, W.Z., Hao, X.P.: Precipitation and erosion characteristics of rainstorm in different pattern on  
848 Loess Plateau, *Journal of Arid Land Resources and Environment*, 13(1), 34-42, (In Chinese), 1999.

849 Kirkby, M.J., Bull, L.J., Poesen, J., Nachtergaele, J., Vandekerckhove, L.: Observed and modelled  
850 distributions of channel and gully heads—with examples from SE Spain and Belgium, *Catena*, 50, 415–434,  
851 [https://doi.org/10.1016/S0341-8162\(02\)00128-5](https://doi.org/10.1016/S0341-8162(02)00128-5), 2003.

852 Li, Binbing., Huang, Lei., Feng, Lin., Li, Peng., Yao, Jingwei., Liu, Fangming., Li, Junli., Tang, Hui.: Gully  
853 sidewall expansion process on loess hill slope erosion, *Journal of Basic Science and Engineering*, 24(6),  
854 1147-1158. (In Chinese), 2016.

855 Li, H., Cruse, R.M., Liu, X.B., Zhang, X.Y.: Effects of topography and land use change on gully development  
856 in typical Mollisol region of Northeast China, *Chinese Geographical Science*, 26, 779-788,  
857 <https://doi.org/10.1007/s11769-016-0837-7>, 2016.

858 Li, M., Song, X.Y., Shen, B., Li, H.Y., Meng, C.X.: Influence of vegetation change on producing runoff and  
859 sediment in gully region of Loess Plateau, *Journal of Northwest Sci-Tech University of AgricuUAure and  
860 Forestry (Natural Science Edition)*, 34, 117-120, (In Chinese), 2006.

861 Li, Y., Mo, Y. Q., Are, K. S., Huang, Z., Guo, H., Tang, C., Abegunrin, T.P., Qin, Z.H, Kang, Z.W., Wang, X.:  
862 Sugarcane planting patterns control ephemeral gully erosion and associated nutrient losses: Evidence from  
863 hillslope observation. *Agriculture, Ecosystems & Environment*, 309, 107289,  
864 <https://doi.org/10.1016/j.agee.2020.107289>, 2021.

865 Li, Z., Zhang, Y., Zhu, Q., He, Y., Yao, W.: Assessment of bank gully development and vegetation coverage on  
866 the Chinese Loess Plateau, *Geomorphology*, 228, 462–469, <https://doi.org/10.1016/j.geomorph.2014.10.005>,  
867 2015.

868 Li, Z., Zheng, F.L., Liu, W.Z., Flanagan, D.C.: Spatial distribution and temporal trends of extreme temperature  
869 and precipitation events on the Loess Plateau of China during 1961–2007, *Quaternary International*, 226(1-2),  
870 92-100, <https://doi.org/10.1016/j.quaint.2010.03.003>, 2010.

871 Ma, Q., Zhang, K., Cao, Z., Wei, M., & Yang, Z.: Soil detachment by overland flow on steep cropland in the  
872 subtropical region of China, *Hydrological Processes*, 34(8), 1810-1820, <https://doi.org/10.1002/hyp.13694>,  
873 2020

874 Martínez-Casasnovas, J.A., Concepción Ramos, M., García-Hernández, David.: Effects of land - use  
875 changes in vegetation cover and sidewall erosion in a gully head of the Penedès region (northeast Spain),  
876 *Earth Surface Processes & Landforms*, 34, 1927-1937, <https://doi.org/10.1002/esp.1870>, 2009.

877 Nazari Samani, A., Ahmadi, H., Mohammadi, A., Ghoddousi, J., Salajegheh, A., Boggs, G., Pishyar, R.:  
878 Factors Controlling Gully Advancement and Models Evaluation (Hableh Rood Basin, Iran), *Water Resources  
879 Management*, 24, 1532–1549, <https://doi.org/10.1007/s11269-009-9512-4>, 2010.

880 Oostwoud-Wijdenes, D., Bryan, R.B.: The significance of gully headcuts as a source of sediment on low-angle  
881 slopes at Baringo, Kenya, and initial control measures, *Advances in Geocology*, 27, 205–231, 1994.

882 Oostwoud-Wijdenes, D., Poesen, J., Vandekerckhove, L., Ghesquiere, M.: Spatial distribution of gully head  
883 activity and sediment supply along an ephemeral channel in a Mediterranean environment, *Catena*, 39, 147–  
884 167, [http://202.194.143.28:80/rwt/SD/https/MSYXTLUQPJUB/10.1016/S0341-8162\(99\)00092-2](http://202.194.143.28:80/rwt/SD/https/MSYXTLUQPJUB/10.1016/S0341-8162(99)00092-2), 2000.

885 Pan, C., Ma, L., Wainwright, J., Shangguan, Z.: Overland flow resistances on varying slope gradients and  
886 partitioning on grassed slopes under simulated rainfall, *Water Resources Research*, 52, 2490–2512,  
887 <https://doi.org/10.1002/2015WR018035>, 2016.

888 Poesen, J., Nachtergaele, J., Verstraeten, G., Valentin, C.: Gully erosion and environmental change:  
889 Importance and research needs, *Catena*, 50, 91-133, [https://doi.org/10.1016/S0341-8162\(02\)00143-1](https://doi.org/10.1016/S0341-8162(02)00143-1), 2003.

890 Qin, Chao., Zheng, Fenli., Wells Robert, R., Xu, Ximeng, Wang, Bin., Zhong, Keyuan.: A laboratory study of  
891 channel sidewall expansion in upland concentrated flows, *Soil and Tillage Research*, 178, 22-31,  
892 <https://doi.org/10.1016/j.still.2017.12.008>, 2018.

893 Reuter, H.I., Nelson, A., Jarvis, A.: An evaluation of void filling interpolation methods for SRTM data,  
894 *International Journal of Geographic Information Science*, 21(9), 983-1008, 2007.

895 Rieke-Zapp, D.H., Nichols, M.H.: Headcut retreat in a semiarid watershed in the southwestern United States  
896 since 1935, *Catena*, 87, 1–10, <https://doi.org/10.1016/j.catena.2011.04.002>, 2011.

897 Rodzik, J., Furtak, T., Zglobicki, W.: The impact of snowmelt and heavy rainfall runoff on erosion rates in a  
898 gully system, Lublin Upland, Poland, *Earth Surface Processes & Landforms*, 34, 1938–1950,  
899 <https://doi.org/10.1002/esp.1882>, 2009.

900 Rouse, H.: *Engineering hydraulics*. Hoboken, NJ: Wiley, 1950.

901 Sanchis, M.P., Torri, D., Borselli, L., Poesen, J.: Climate effects on soil erodibility, *Earth Surface Processes &*  
902 *Landforms*, 33, 1082–1097, <https://doi.org/10.1002/esp.1604>, 2008.

903 Shen, N., Wang, Z., Zhang, Q., Chen, H., Wu, B.: Modelling soil detachment capacity by rill flow with  
904 hydraulic variables on a simulated steep loessial hillslope, *Hydrology Research*, 50(1), 85-98,  
905 <https://doi.org/10.2166/nh.2018.037>, 2018.

906 Shi, Q.H., Wang, W.L., Guo, M.M., Chen, Z.X., Feng, L.Q., Zhao, M., Xiao, H.: The impact of flow discharge  
907 on the hydraulic characteristics of headcut erosion processes in the gully region of the Loess Plateau,  
908 *Hydrological processes*, 34, 718-729, <https://doi.org/10.1002/hyp.13620>, 2020.

909 Shi, Q., Wang, W., Zhu, B., Guo, M.: Experimental study of hydraulic characteristics on headcut erosion and  
910 erosional response in the tableland and gully regions of China, *Soil Science Society of America Journal*, 84,  
911 700–716, <https://doi.org/10.1002/saj2.20068>, 2020.

912 Sidorchuk, A.: The potential of gully erosion on the Yamal peninsula, West Siberia. *Sustainability*, 12(1), 260,  
913 <https://doi.org/10.3390/su12010260>, 2020.

914 Stein, O., Julien, P., Alonso, C.: Mechanics of jet scour downstream of a headcut, *Journal of Hydraulic*  
915 *Research*, 31, 723–738, <https://doi.org/10.1080/00221689309498814>, 1993.

916 Su, Z.A., Xiong, D.H., Dong, Y.F., Zhang, B.J., Zhang, S., Zheng, X.Y., Fang, H.D.: Hydraulic properties  
917 of concentrated flow of a bank gully in the dry - hot valley region of southwest China, *Earth Surface*  
918 *Processes and Landforms*, 40, 1351 - 1363. <https://doi.org/10.1002/esp.3724>, 2015.

919 Su, Z.A., Xiong, D.H., Dong, Y.F., Li, J.J., Yang, D., Zhang, J.H., He, G.X.: Simulated headward erosion of  
920 bank gullies in the Dry-hot Valley Region of southwest China, *Geomorphology*, 204, 532–541,  
921 <https://doi.org/10.1016/j.geomorph.2013.08.033>, 2014.

922 Sun, W.Y., Mu, X.M., Song, X.Y., Wu, D., Cheng, A.F., Qiu, B.: Changes in extreme temperature and  
923 precipitation events in the Loess Plateau (China) during 1960–2013 under global warming, *Atmospheric*  
924 *Research*, 168, 33-48, <https://doi.org/10.1016/j.atmosres.2015.09.001>, 2016.

925 Thompson, J.R.: Quantitative effect of watershed variables on rate of gully - head advancement. *Transactions*  
926 *of the ASABE*, 7, 54 - 55, <https://doi.org/10.13031/2013.40694>, 1964.

927 Torri, D., Poesen, J.: A review of topographic threshold conditions for gully head development in different  
928 environments, *Earth-Science Reviews*, 130, 73–85, <https://doi.org/10.1016/j.earscirev.2013.12.006>, 2014.

929 Valentin, C., Poesen, J., Li, Y.: Gully erosion: Impacts, factors and control, *Catena*, 63, 132–153,  
930 <https://doi.org/10.1016/j.catena.2005.06.001>, 2005.

931 Vandekerckhove, L., Poesen, J., Govers, G.: Medium-term gully headcut retreat rates in southeast Spain  
932 determined from aerial photographs and ground measurements, *Catena*, 50(2-4), 329-352,  
933 [https://doi.org/10.1016/S0341-8162\(02\)00132-7](https://doi.org/10.1016/S0341-8162(02)00132-7), 2003.

934 Vandekerckhove, L., Poesen, J., Wijdenes, D.O., Nachtergaele, J., Tomás de Figueiredo.: Thresholds for gully  
935 initiation and sedimentation in Mediterranean Europe, *Earth Surface Processes & Landforms*, 25(11),  
936 1201-1220, [https://doi.org/10.1002/1096-9837\(200010\)25:11<1201::AID-ESP131>3.0.CO;2-L](https://doi.org/10.1002/1096-9837(200010)25:11<1201::AID-ESP131>3.0.CO;2-L), 2015.

937 Vanmaercke, M., Poesen, J., Mele, B.V., Demuzere, M., Bruynseels, A., Golosov, V., ... Yermolaev, O.: How  
938 fast do gully headcuts retreat?, *Earth - Science Reviews*, 154, 336 - 355,  
939 <https://doi.org/10.1016/j.earscirev.2016.01.009>, 2016.

940 Vannoppen, W., Vanmaercke, M., De Baets, S., Poesen, J.: A review of the mechanical effects of plant roots on  
941 concentrated flow erosion rates, *Earth - Science Reviews*, 150, 666 - 678,  
942 <https://doi.org/10.1016/j.earscirev.2015.08.011>, 2015.

943 Vanwalleghem, T., Bork, H.R., Poesen, J., Schmidtchen, G., Dotterweich, M., Nachtergaele, J., Bork, H.,  
944 Deckers, J., Brüsck, B., Bungeneers, J., De Bie, M.: Rapid development and infilling of a buried gully under  
945 cropland, Central Belgium, *Catena*, 63, 221–243, <https://doi.org/10.1016/j.catena.2005.06.005>, 2005.

946 Vanwalleghem, T., Van Den Eeckhaut, M., Poesen, J., Deckers, J., Nachtergaele, J., Van Oost, K., Slenters, C.:  
947 Characteristics and controlling factors of old gullies under forest in a temperate humid climate: a case study  
948 from the Meerdaal Forest (Central Belgium), *Geomorphology*, 56(1), 15–29,  
949 [https://doi.org/10.1016/S0169-555X\(03\)00043-6](https://doi.org/10.1016/S0169-555X(03)00043-6), 2003.

950 Wells, R.R., Alonso, C.V., Bennett, S.J.: Morphodynamics of Headcut Development and Soil Erosion in  
951 Upland Concentrated Flows, *Soil Science Society of America Journal*, 73, 521–530.  
952 <https://doi.org/10.2136/sssaj2008.0007>, 2009a.

953 Wells, R.R., Bennett, S.J., Alonso, C.V.: Effect of soil texture, tailwater height, and pore - water pressure on  
954 the morphodynamics of migrating headcuts in upland concentrated flows, *Earth Surface Processes and*  
955 *Landforms*, 34, 1867 - 1877, <https://doi.org/10.1002/esp.1871>, 2009b.

956 Wells, R.R., Momm, H.G., Rigby, J.R., Bennett, S.J., Bingner, R.L., Dabney, S.M.: An empirical investigation  
957 of gully widening rates in upland concentrated flows, *Catena*, 101, 114-121,  
958 <https://doi.org/10.1016/j.catena.2012.10.004>, 2013.

959 Wen, X., Wu, X., Gao, M.: Spatiotemporal variability of temperature and precipitation in Gansu province  
960 (northwest China) during 1951–2015, *Atmospheric Research*, 197, 132-149,  
961 <https://doi.org/10.1016/j.atmosres.2017.07.001>, 2017.

962 Wen, Y., Kasielke, T., Li, H., Zhang, B., Zepp, H.: May agricultural terraces induce gully erosion? a case study  
963 from the black soil region of northeast China. *Science of The Total Environment*, 750(4), 141715,  
964 <https://doi.org/10.1016/j.scitotenv.2020.141715>, 2020.

965 Wu, Bing., Wang, Zhanli., Zhang, Qingwei., Shen, Nan., Liu, June., Wang, Sha.: Evaluation of shear stress  
966 and unit stream power to determine the sediment transport capacity of loess materials on different slopes,  
967 *Journal of Soil & Sediments*, 18, 116–127, <https://doi.org/10.1007/s11368-017-1758-5>, 2018.

968 Wu, B., Wang, Z., Shen, N., Wang, S.: Modelling sediment transport capacity of rill flow for loess sediments  
969 on steep slopes, *Catena*, 147, 453-462, <https://doi.org/10.1016/j.catena.2016.07.030>, 2016.

970 Xia, L., Song, X.Y., Fu, N., Li, H.Y., Li, Y.L.: Impacts of land use change and climate variation on green water  
971 in the Loess Plateau Gully Region—A case study of Nanxiaohegou basin, *Journal of Hydraulic Engineering*,  
972 48(6), 678-688, (In Chinese), 2017.

973 Xu, J.Z., Li, H., Liu, X.B., Hu, W., Yang, Q.N., Hao, Y.F., Zhen, H.C., Zhang, X.Y.: Gully Erosion Induced by  
974 SnowmeUA in Northeast China: A Case Study, *Sustainability*, 11, <https://doi.org/10.3390/su11072088>, 2019.

975 Xu, X.M., Zheng, F.L., Wilson, G.V., Wu, M.: Upslope inflow, hillslope gradient and rainfall intensity impacts  
976 on ephemeral gully erosion, *Land Degradation & Development*, 28, 2623-2635  
977 <https://doi.org/10.1002/ldr.2825>, 2017.

978 Xu, X.M., Zheng, F.L., Qin, C., Wu, H.Y., Wilson, G.V.: Impact of cornstalk buffer strip on hillslope soil  
979 erosion and its hydrodynamic understanding, *Catena*, 149, 417-425,  
980 <https://doi.org/10.1016/j.catena.2016.10.016>, 2017.

981 Xu, X.M., Wang, H.B., Zhao, J.Y., Liu, X.J.: Dynamic variation of soil erosion of Nanxiaohegou small  
982 watershed during 2004-2016, *Soil and Water Conservation in China*, 443(2), 59-61, (In Chinese), 2019.

983 Yang, C.T.: Potential energy and stream morphology, *Water Resource Research*, 7(2), 311-223,  
984 <https://doi.org/10.1029/WR007i002p00311>, 1971a.

985 Yang, C.T.: On river meanders, *Journal of Hydrology*, 13, 231-253,  
986 [https://doi.org/10.1016/0022-1694\(71\)90226-5](https://doi.org/10.1016/0022-1694(71)90226-5), 1971b.

987 Zhang, B.J., Xiong, D.H., Su, Z.A., Yang, D., Dong, Y.F., Xiao, L., Zhang, S., Shi, L.T.: Effects of initial step  
988 height on the headcut erosion of bank gullies: a case study using a 3D photo-reconstruction method in the  
989 Dry-hot Valley region of southwest China, *Physical Geography*, 37, 409-429,  
990 <https://doi.org/10.1080/02723646.2016.1219939>, 2016.

991 Zhang, B.J., Xiong, D.H., Zhang G.H., Zhang, S., Wu, H., Yang, D., Xiao, L., Dong, Y.F., Su, Z.A., Lu, X.N.:  
992 Impacts of headcut height on flow energy, sediment yield and surface landform during bank gully erosion  
993 processes in the Yuanmou Dry - hot Valley region, southwest China, *Earth Surface Processes & Landforms*,  
994 43(10), 2271-2282, <https://doi.org/10.1002/esp.4388>, 2018.

995 Zhang, H.X.: The characteristics of hard rain and its distribution over the Loess Plateau, *Acta Geographica*  
996 *Sinica*, 38, 416-425, (In Chinese), 1983.

997 Zhang, G.H., Liu, Y.M., Han, Y.F., Zhang, X.C.: Sediment transport and soil detachment on steep slopes: I.  
998 transport capacity estimation, *Soil Science Society of America Journal*, 73, 1291-1297,  
999 <https://doi.org/10.2136/sssaj2008.0145>, 2009.

1000 Zhang, X., Fan, J., Liu, Q., Xiong D.: The contribution of gully erosion to total sediment production in a small  
1001 watershed in Southwest China, *Physical Geography*, 39(3), 1-18,  
1002 <https://doi.org/10.1080/02723646.2017.1356114>, 2018.

1003 Zhao, A.C.: Analysis of control models of typical small watershed in gully area of Loess Plateau, the east part  
1004 of Gansu Province, *Research of Soil and Water Conservation*, 1, 45-49, (In Chinese), 1994.

1005 Zhu, T.X.: Gully and tunnel erosion in the hilly Loess Plateau region, China, *Geomorphology*, 153, 144-155,  
1006 <https://doi.org/10.1016/j.geomorph.2012.02.019>, 2012.